

THE MOSDEF SURVEY: ELECTRON DENSITY AND IONIZATION PARAMETER AT $z \sim 2.3$ *

RYAN L. SANDERS¹, ALICE E. SHAPLEY¹, MARISKA KRIEK², NAVEEN A. REDDY^{3,5}, WILLIAM R. FREEMAN³, ALISON L. COIL⁴, BRIAN SIANA³, BAHRAM MOBASHER³, IRENE SHIVAEI³, SEDONA H. PRICE², AND LAURA DE GROOT³

Draft version November 7, 2018

ABSTRACT

Using observations from the MOSFIRE Deep Evolution Field (MOSDEF) survey, we investigate the physical conditions of star-forming regions in $z \sim 2.3$ galaxies, specifically the electron density and ionization state. From measurements of the [O II] $\lambda\lambda 3726, 3729$ and [S II] $\lambda\lambda 6716, 6731$ doublets, we find a median electron density of $\sim 250 \text{ cm}^{-3}$ at $z \sim 2.3$, an increase of an order of magnitude compared to measurements of galaxies at $z \sim 0$. While $z \sim 2.3$ galaxies are offset towards significantly higher O_{32} values relative to local galaxies at fixed stellar mass, we find that the high-redshift sample follows a similar distribution to the low-metallicity tail of the local distribution in the O_{32} vs. R_{23} and $O3N2$ diagrams. Based on these results, we propose that $z \sim 2.3$ star-forming galaxies have the same ionization parameter as local galaxies at fixed metallicity. In combination with simple photoionization models, the position of local and $z \sim 2.3$ galaxies in excitation diagrams suggests that there is no significant change in the hardness of the ionizing spectrum at fixed metallicity from $z \sim 0$ to $z \sim 2.3$. We find that $z \sim 2.3$ galaxies show no offset compared to low-metallicity local galaxies in emission line ratio diagrams involving only lines of hydrogen, oxygen, and sulfur, but show a systematic offset in diagrams involving [N II] $\lambda 6584$. We conclude that the offset of $z \sim 2.3$ galaxies from the local star-forming sequence in the [N II] BPT diagram is primarily driven by elevated N/O at fixed O/H compared to local galaxies. These results suggest that the local gas-phase and stellar metallicity sets the ionization state of star-forming regions at $z \sim 0$ and $z \sim 2$.

Subject headings: galaxies: evolution — galaxies: ISM — galaxies: high-redshift

1. INTRODUCTION

The star-formation rate density of the universe peaked at $z \sim 2$ (Hopkins & Beacom 2006; Madau & Dickinson 2014). Understanding the physical conditions in star-forming regions during this epoch is essential for a complete description of the evolution of the stellar and gaseous content of galaxies. One method of probing these conditions is observing recently formed stars embedded in ionized gas clouds. Rest-frame optical emission lines from HII regions encode a significant amount of information about the ionizing source and the physical conditions of the ionized gas. A small set of physical properties appears to determine the strong optical emission line fluxes produced in HII regions, including the chemical abundance, the shape and normalization of the ionizing spectrum, the ionization state of the gas, and the gas density (Dopita & Evans 1986; Kewley & Dopita 2002; Dopita et al. 2006a,b).

email: rlsand@astro.ucla.edu

* Based on data obtained at the W.M. Keck Observatory, which is operated as a scientific partnership among the California Institute of Technology, the University of California, and NASA, and was made possible by the generous financial support of the W.M. Keck Foundation.

¹ Department of Physics & Astronomy, University of California, Los Angeles, 430 Portola Plaza, Los Angeles, CA 90095, USA

² Astronomy Department, University of California, Berkeley, CA 94720, USA

³ Department of Physics & Astronomy, University of California, Riverside, 900 University Avenue, Riverside, CA 92521, USA

⁴ Center for Astrophysics and Space Sciences, University of California, San Diego, 9500 Gilman Dr., La Jolla, CA 92093-0424, USA

⁵ Alfred P. Sloan Fellow

Over the past decade, a body of work has been produced showing that galaxies at $z \sim 1 - 2$ display certain emission line ratios that are atypical of local star-forming galaxies (e.g., Shapley et al. 2005; Erb et al. 2006; Liu et al. 2008; Hainline et al. 2009; Holden et al. 2014; Nakajima & Ouchi 2014; Steidel et al. 2014; Shapley et al. 2015). These observations suggest that at least some of the physical conditions that influence emission line production in star-forming regions must be different in high-redshift galaxies. It is well-established that galaxies at $z > 1$ have lower metallicities than local galaxies at fixed stellar mass (Erb et al. 2006; Maiolino et al. 2008; Belli et al. 2013; Henry et al. 2013; Stott et al. 2013; Cullen et al. 2014; Steidel et al. 2014; Troncoso et al. 2014; Sanders et al. 2015). The electron density and ionization state of the gas also affect emission line production, but are less well-constrained and have fewer measurements at $z > 1$.

Estimates of the electron density at $z \sim 2$ have suggested that densities in high-redshift star-forming regions are significantly higher than what is typically observed locally (Hainline et al. 2009; Lehnert et al. 2009; Bian et al. 2010; Shirazi et al. 2014). However, the small and heterogeneous galaxy samples used in these studies leave the electron density of typical star-forming regions at $z \sim 2$ poorly constrained. Electron density estimates in a large, representative sample of $z \sim 2$ galaxies are needed to obtain robust constraints on the typical electron densities at high redshift.

The typical ionization state of gas in $z \sim 2$ star-forming regions appears to differ from that of local star-forming regions. Galaxies at $z > 1$ display higher values of [O III] $\lambda 5007/H\beta$ and

$[\text{O III}]\lambda\lambda 4959, 5007/[\text{O II}]\lambda\lambda 3726, 3729$ than are typical of local galaxies, leading to the conclusion that high-redshift galaxies have higher ionization parameters than local galaxies, on average (Brinchmann et al. 2008; Hainline et al. 2009; Holden et al. 2014; Nakajima & Ouchi 2014; Shirazi et al. 2014). A systematic investigation of the variation of the ionization state with other galaxy properties at $z \sim 2$ is necessary to uncover the cause of these elevated ionization parameters.

In this paper, we investigate the physical properties of star-forming regions at $z \sim 2.3$, specifically the electron density and ionization state, using a large, systematically-selected sample from the MOSFIRE Deep Evolution Field (MOSDEF) survey. Until recently, samples of rest-frame optical spectra of $z \sim 2$ galaxies were small, heterogeneous, and usually included only a subset of the strongest nebular emission lines. These samples reflected the difficulty of obtaining spectra of faint galaxies in the near-infrared, typically using long-slit spectrographs covering one near-infrared band at a time. With the development of sensitive near-infrared detectors and multi-object near-infrared spectrographs on 8-10 m class telescopes, large samples of $z \sim 2$ galaxies with rest-frame optical emission line measurements across multiple near-infrared bands are being assembled for the first time (Steidel et al. 2014; Kriek et al. 2015). These spectra contain a wealth of diagnostic information that probes the star-formation rate (SFR), dust attenuation, gas density, ionization state, chemical enrichment, and more for $z \sim 2$ galaxies. Building on the work of Shapley et al. (2015), we utilize the full range of strong optical emission lines to investigate the physical properties of HII regions using various diagnostic line ratios. In combination with rich datasets at lower redshifts, such measurements make it possible to understand how conditions in star-forming regions have evolved over the past ~ 10 Gyr of cosmic history.

Changes in the physical conditions of star-forming gas are thought to be the cause of the offset of $z > 1$ galaxies from the local sequence of star-forming galaxies in the $[\text{O III}]\lambda 5007/\text{H}\beta$ vs. $[\text{N II}]\lambda 6584/\text{H}\alpha$ excitation diagram (Shapley et al. 2005; Liu et al. 2008; Hainline et al. 2009; Steidel et al. 2014; Shapley et al. 2015). It has been proposed that this offset is caused by higher gas density/pressure (Kewley et al. 2013a), systematically harder ionizing spectra (Steidel et al. 2014), higher ionization parameters (Brinchmann et al. 2008), or an enhancement in the N/O ratio (Masters et al. 2014; Shapley et al. 2015) in high-redshift galaxies in comparison to what is typically observed in the local universe. The offset could be caused by a combination of some or all of these parameters. By characterizing the differences in the density and ionization state of $z \sim 2$ and $z \sim 0$ star-forming galaxies, as we do here, we can gain a better understanding of which parameters drive the offset in the $[\text{O III}]\lambda 5007/\text{H}\beta$ vs. $[\text{N II}]\lambda 6584/\text{H}\alpha$ excitation diagram, and the relative importance of each. Determining the evolution of these properties with redshift also has implications for the applicability of local metallicity calibrations at $z \sim 1 - 2$.

This paper is structured as follows. In Section 2, we briefly describe the MOSDEF survey, along with the observations, reduction, and measurements. We estimate the typical electron density in $z \sim 2.3$ star-forming re-

gions and characterize the evolution of density with redshift in Section 3. In Section 4, we investigate the ionization state of $z \sim 2.3$ galaxies and its dependence on global galaxy properties and metallicity indicators. We propose a scenario in which galaxies at $z \sim 2.3$ have the same ionization parameter as galaxies at $z \sim 0$ at fixed metallicity. In Section 5, we provide evidence supporting our proposed scenario and discuss the implications for the interpretation of observed emission-line ratios of $z \sim 2.3$ galaxies, including the offset in the $[\text{O III}]\lambda 5007/\text{H}\beta$ vs. $[\text{N II}]\lambda 6584/\text{H}\alpha$ diagram. We conclude by summarizing our main results in Section 6.

We adopt the following shorthand abbreviations to refer to commonly used emission line ratios:

$$\text{O}_{32} = [\text{O III}]\lambda\lambda 4959, 5007/[\text{O II}]\lambda\lambda 3726, 3729 \quad (1)$$

$$\text{R}_{23} = ([\text{O III}]\lambda\lambda 4959, 5007 + [\text{O II}]\lambda\lambda 3726, 3729)/\text{H}\beta \quad (2)$$

$$\text{O3N2} = ([\text{O III}]\lambda 5007/\text{H}\beta)/([\text{N II}]\lambda 6584/\text{H}\alpha) \quad (3)$$

$$\text{N2} = [\text{N II}]\lambda 6584/\text{H}\alpha \quad (4)$$

Throughout this paper, the term ‘‘metallicity’’ is used synonymously with gas-phase oxygen abundance (O/H) unless otherwise mentioned. We adopt a Λ -CDM cosmology with $H_0 = 70 \text{ km s}^{-1} \text{ Mpc}^{-1}$, $\Omega_m = 0.3$, and $\Omega_\Lambda = 0.7$.

2. OBSERVATIONS

We use data taken during the first two years (2012B-2014A) of the MOSFIRE Deep Evolution Field survey. We briefly describe the MOSDEF survey, observations, reduction, and derived quantities here. Full technical details of the survey strategy, observations, reduction pipeline, and sample characteristics can be found in Kriek et al. (2015). We additionally use data from the Sloan Digital Sky Survey (SDSS; York et al. 2000) Data Release 7 (DR7; Abazajian et al. 2009) catalog to select local comparison samples for studying evolution with redshift. Emission-line measurements and galaxy properties are taken from the MPA-JHU catalog of measurements for SDSS DR7.⁶

2.1. The MOSDEF Survey

The MOSDEF survey is an ongoing multi-year project in which we are obtaining rest-frame optical spectra of galaxies at $z \sim 1.4 - 3.8$ with the goal of transforming the understanding of the gaseous, stellar, dust, and black hole content of galaxies at that epoch in cosmic history. This project utilizes the Multi-Object Spectrometer For Infra-Red Exploration (MOSFIRE; McLean et al. 2012) on the 10 m Keck I telescope. Potential for scientific gain from the MOSDEF dataset is maximized by targeting objects in the AEGIS, COSMOS, and GOODS-N extragalactic fields with extensive multi-wavelength ancillary data. These data include *Hubble Space Telescope* (HST) imaging from the Cosmic Assembly Near-infrared Deep Extragalactic Legacy Survey (CANDELS; Grogin et al. 2011; Koekemoer et al. 2011) and grism spectroscopy from the 3D-HST survey (Brammer et al. 2012a), as well as observations from *Chandra*, *Spitzer*, *Herschel*, VLA,

⁶ Available at <http://www.mpa-garching.mpg.de/SDSS/DR7/>

and ground-based observatories in the optical and near-infrared.

In the MOSDEF survey, we target galaxies in the three redshift windows $1.37 \leq z \leq 1.70$, $2.09 \leq z \leq 2.61$, and $2.95 \leq z \leq 3.80$, where the redshift ranges are selected such that strong optical emission-line features fall within windows of atmospheric transmission in the Y, J, H, or K near-infrared bands. This targeting strategy leads to coverage of [OII] $\lambda\lambda$ 3726,3729, H β , and [O III] $\lambda\lambda$ 4959,5007 for all three redshift bins, as well as [N II] $\lambda\lambda$ 6548,6584, H α , and [S II] $\lambda\lambda$ 6716,6731 for the $z \sim 1.5$ and $z \sim 2.3$ bins. These strong optical emission lines are powerful diagnostics for determining physical properties of galaxies including dust content (Reddy et al. 2015), star-formation rate (SFR) (Shivaei et al. 2015), chemical abundance (Sanders et al. 2015), gas density, ionization state, and black hole activity (Coil et al. 2015). Targets are selected from the 3D-HST photometric and spectroscopic catalogs (Skelton et al. 2014) based on their rest-frame optical (observed H-band) magnitudes and redshifts (grism or spectroscopic redshifts, if available, and photometric redshifts otherwise). Galaxies are targeted down to *HST*/WFC3 F160W AB magnitudes of 24.0 at $z \sim 1.5$, 24.5 at $z \sim 2.3$, and 25.0 at $z \sim 3.4$. Targets with pre-existing spectroscopic redshifts, including grism redshifts or ground-based spectroscopic redshifts, are given higher priority, as are galaxies with brighter F160W magnitudes. As described in Kriek et al. (2015), the MOSDEF survey will obtain spectra for ~ 1500 galaxies when complete, with ~ 750 at $z \sim 2.3$, and ~ 400 each at $z \sim 1.5$ and $z \sim 3.4$.

2.2. Observations and Reduction

We use data from the first two observing seasons of the MOSDEF survey. Observations were taken on ten observing runs from 2012 December to 2014 May, during which 21 MOSFIRE masks were observed. The first observing run, taking place in 2012 December, was a pilot program during which we observed one mask each in the GOODS-S and UDS CANDELS fields due to the limited visibility of the primary target fields. This work focuses on the $z \sim 2.3$ redshift bin, and, accordingly, we only describe the observations for this redshift interval. MOSDEF targets at $z \sim 2.3$ are observed in the J, H, and K near-infrared bands, with [OII] $\lambda\lambda$ 3726,3729 in J, H β and [O III] $\lambda\lambda$ 4959,5007 in H, and [N II] $\lambda\lambda$ 6548,6584, H α , and [S II] $\lambda\lambda$ 6716,6731 in K. Observed MOSFIRE masks each contain ~ 30 slits with widths of $0''7$, yielding a spectral resolution of 3300, 3650, and 3600 in J, H, and K bands, respectively. One slit on each mask was placed on a reference star used in the reduction. Masks were typically observed using an ABA'B' dither pattern, with individual exposure times at each dither position of 120 seconds in J and H, and 180 seconds in K. The total exposure time per filter per mask was typically 2 hours.

The raw data were reduced using a custom IDL pipeline developed by the MOSDEF team and described in detail in Kriek et al. (2015). The raw science frames were flatfielded and sky subtracted, cosmic rays were identified and masked, and the two-dimensional spectra were rectified. Individual exposures were combined and the resulting spectrum was flux calibrated. Shape correction due to varying spectral response with wavelength and telluric absorption features was achieved using ob-

servations of B8-A1 V standard stars matched to the typical air mass of science observations. Flux calibration was performed by requiring the flux density of the reference star on a mask to match its cataloged broadband photometry. For each slit, a two-dimensional error spectrum was produced accounting for Poisson counting uncertainty for the observed intensity per pixel and read noise. From the two-dimensional science and error spectra, one-dimensional spectra were produced using the optimal extraction technique. Spectra for any detected objects serendipitously falling on the slit were also extracted (Freeman et al., in prep.). The final flux calibration was achieved by applying a slit-loss correction term to the extracted science spectra on an individual basis. The fraction of light from an object falling outside of the slit was estimated using a two-dimensional Gaussian fit to the F160W image of a galaxy convolved with the seeing estimate for each mask and filter. The flux calibration was checked by verifying that objects with detected continuum had flux densities consistent with broadband photometry.

2.3. Measurements and Derived Quantities

Emission line fluxes were measured by fitting Gaussian profiles to emission lines in the one-dimensional spectra, while the uncertainty on the emission line flux was based on the 68th percentile width of the distribution of measured fluxes obtained by perturbing the spectrum according to the error spectrum and refitting the emission line 1,000 times (Reddy et al. 2015). All emission lines were fit with a single Gaussian profile except for the cases of [N II] $\lambda\lambda$ 6548,6584 and H α , fit simultaneously with a triple Gaussian, and [O II] $\lambda\lambda$ 3726,3729, fit simultaneously with a double Gaussian and described in detail in Section 3.2. The highest signal-to-noise emission line of each object, typically H α or [O III] λ 5007, was used to constrain the centroid and width of the other emission lines and measure the redshift. Stellar masses were estimated by utilizing the stellar population synthesis models of Conroy et al. (2009) with the SED-fitting code FAST (Kriek et al. 2009) using the measured MOSDEF spectroscopic redshifts and broadband photometric catalogs assembled by the 3D-HST team (Skelton et al. 2014) spanning observed optical to mid-infrared. The Calzetti et al. (2000) attenuation curve and a Chabrier (2003) IMF were assumed. Uncertainties on the stellar masses were estimated using a Monte Carlo method where the input photometry was perturbed according to the errors and the SED was refit 500 times (Kriek et al. 2015). SFRs were estimated from dust-corrected H α luminosities using the Kennicutt (1998) calibration converted to a Chabrier (2003) IMF (Shivaei et al. 2015). Balmer line fluxes were first corrected for stellar Balmer absorption using the best-fit SEDs (Reddy et al. 2015), and the dust correction was estimated using H α /H β assuming an intrinsic ratio of 2.86 and the Cardelli et al. (1989) extinction curve.

Emission line fluxes are dust-corrected in line ratios involving lines significantly separated in wavelength (O $_{32}$ and R $_{23}$), but are not dust-corrected in line ratios featuring lines with a close wavelength spacing (O3N2, N2, [O III]/H β , and [S II]/H α). Uncertainties on emission line ratios are estimated using a monte carlo method by perturbing each individual line flux according to its un-

certainty, recalculating the emission line ratio, and repeating the preceding steps 10,000 times to build up a distribution of perturbed line ratios. The uncertainty on the line ratio is determined from the 68th percentile width of this distribution. Error estimates on O_{32} and R_{23} values include uncertainty in the Balmer decrement by recalculating the dust correction for each realization.

After removing those objects identified as AGN based on their X-ray or IR properties (Coil et al. 2015), there are 225 star-forming galaxies confirmed to be in the $z \sim 2.3$ redshift interval spanning a stellar mass range of $10^{8.97} - 10^{11.64} M_{\odot}$ with a median stellar mass of $10^{9.99} M_{\odot}$. The subset of these galaxies with H α and H β detected (67%) has SFRs spanning $1.61 - 323 M_{\odot}/\text{yr}$ with a median SFR of $21.6 M_{\odot}/\text{yr}$, and spans a range in stellar mass of $10^{8.97} - 10^{11.22} M_{\odot}$ with a median stellar mass of $10^{10.0} M_{\odot}$. Shivaie et al. (2015) have shown that the SFR- M_{*} relation of MOSDEF $z \sim 2.3$ star-forming galaxies is similar to what is observed in other studies that employ different SFR indicators (see their Figure 8). Accordingly, the $z \sim 2.3$ star-forming galaxy population recovered by the MOSDEF survey appears to be representative of the range of SFRs spanned by star-forming galaxies at these stellar masses and this redshift (Reddy et al. 2012; Whitaker et al. 2014; Shivaie et al. 2015).

3. ELECTRON DENSITIES

The electron density of star-forming regions affects the fluxes of collisionally excited lines and is thus an important quantity to measure as an input parameter to photoionization models.⁷ The electron density can be estimated using the line fluxes of components of a doublet of a single species in which the two levels of the doublet have different collision strengths and radiative transition probabilities (Osterbrock & Ferland 2006). The flux observed in each component of the doublet is dependent on the relative population in each energy level, which is sensitive to the density of electrons available for collisional excitation and de-excitation. Rest-frame optical spectra provide access to two strong emission line doublets useful for estimating the electron density, namely [O II] $\lambda\lambda 3726, 3729$ and [S II] $\lambda\lambda 6716, 6731$. We use the ratios of the components of these doublets to estimate densities for local SDSS galaxies and high-redshift galaxies from the MOSDEF sample.

3.1. Methods

We have written a python script that solves a 5-level atom approximation of the O II and S II ions for the relative populations in the second and third energy levels. Decays from these two energy levels produce the two components of the [O II] $\lambda\lambda 3726, 3729$ and [S II] $\lambda\lambda 6716, 6731$ doublets. We set up a detailed balance of transitions into and out of each of the five energy levels via radiative decay and collisional excitation and de-excitation, assuming the system is in thermal equilibrium. The detailed balance provides a system of equations that can be solved for the relative populations at a given density. Given n_2 and n_3 , the relative populations

in the second and third energy levels, the ratio of the line fluxes is given by

$$\frac{F_3}{F_2} = \frac{E_{31}n_3A_{31}}{E_{21}n_2A_{21}} \approx \frac{n_3A_{31}}{n_2A_{21}} \quad (5)$$

where F_i is the emission line intensity of decay from the i th level to the ground state, E_{i1} is the energy difference between the i th level and the ground state, and A_{i1} is the transition probability of the i th level to the ground state.

Calculating the proper emission line ratio corresponding to a given density requires accurate knowledge of the transition probabilities and collision strengths of each transition between the five energy levels. Recent investigations (Nicholls et al. 2013; Dopita et al. 2013) have suggested advantages in using the most up-to-date collision strength and transition probability atomic data instead of outdated values included in the IRAF routine *temden* (Shaw & Dufour 1994). Motivated by these studies, we adopt the effective collision strengths from Tayal (2007) for O II and Tayal & Zatsarinny (2010) for S II, while the transition probabilities for both species are taken from the NIST MCHF database (Fischer & Tachiev 2014). Using other estimates of the collision strengths and transition probabilities can change the calculated electron densities by up to $\sim 30\%$. We verified that our script can exactly match IRAF *temden* when using the same atomic data.

The effective collision strengths have some temperature dependence and have been calculated over a range of electron temperatures from 2000 K to 100,000 K for O II and 5000 K to 100,000 K for S II. We adopt the effective collision strengths calculated with an electron temperature of 10,000 K, a representative equilibrium temperature of HII regions that are neither metal-rich nor metal-poor. We note that the temperature dependence is not negligible. Assuming an electron temperature of 7,000 K yields electron densities that are $\sim 15 - 20\%$ lower at a fixed line ratio, while an electron temperature of 15,000 K gives densities that are higher by the same amount. Because we assume a fixed electron temperature of 10,000 K, we are likely overestimating the electron density in metal-rich galaxies, and underestimating the density in galaxies that are metal-poor. However, the uncertainty introduced by this assumption is smaller than the typical measurement uncertainty for individual $z \sim 2.3$ galaxies.

We calculate the line ratios [O II] $\lambda 3729/\lambda 3726$ and [S II] $\lambda 6716/\lambda 6731$ over a range of electron densities of $\log\left(\frac{n_e}{\text{cm}^{-3}}\right) = 0$ to 5 in 0.01 dex steps. The result is well fit by a function of the form

$$R(n_e) = a \frac{b + n_e}{c + n_e} \quad (6)$$

where $R = [\text{O II}]\lambda 3729/\lambda 3726$ or $[\text{S II}]\lambda 6716/\lambda 6731$ is the line flux ratio. The best-fit parameters using up-to-date atomic data are shown in Table 1 for [O II] and [S II]. Figure 1 shows this diagnostic relation for the new atomic data (black) and the relation from IRAF *temden* (red) for both [O II] (solid) and [S II] (dashed). It can be seen in Figure 1 that the line ratio asymptotically approaches a theoretical maximum value in the low-density limit and a theoretical minimum value in the high-density

⁷ The models described in Section 5 actually use the hydrogen gas density as an input parameter. In HII regions, the hydrogen gas is fully ionized such that the electron density is a good proxy for the hydrogen gas density.

Table 1
Coefficients and limiting line ratios for [O II] and [S II] in equations 6 and 7

R	a	b	c	R_{\min}^a	R_{\max}^b
[O II] $\lambda\lambda 3729/\lambda 3726$	0.3771	2,468	638.4	0.3839	1.4558
[S II] $\lambda\lambda 6716/\lambda 6731$	0.4315	2,107	627.1	0.4375	1.4484

^aTheoretical minimum line ratio calculated in the high-density limit of $100,000 \text{ cm}^{-3}$

^bTheoretical maximum line ratio calculated in the low-density limit of 1 cm^{-3}

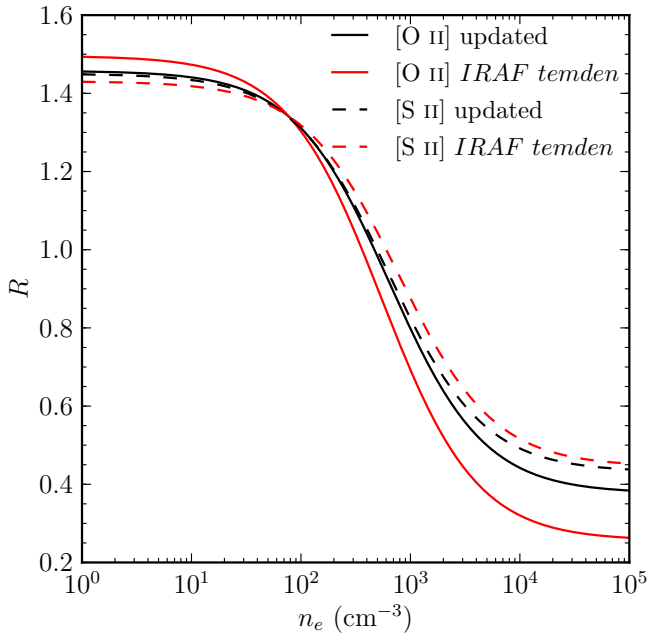


Figure 1. R vs. n_e curves (equation 6) from IRAF temden (red) and our five-level atom python script using new atomic data (black), where $R = [\text{O II}]\lambda\lambda 3729/\lambda 3726$ (solid) or $[\text{S II}]\lambda\lambda 6716/\lambda 6731$ (dashed).

limit. We calculate the theoretical maximum and minimum line ratios at densities of 1 cm^{-3} and $100,000 \text{ cm}^{-3}$, respectively, and show these values in Table 1. Inverting equation 6 yields the density as a function of the line ratio

$$n_e(R) = \frac{cR - ab}{a - R} \quad (7)$$

which we use to calculate electron densities. Uncertainties on individual density measurements are estimated by converting the upper and lower 68th percentile uncertainties on the line ratio into electron densities, where the upper (lower) uncertainty in line ratio corresponds to the lower (upper) uncertainty in density.

3.2. Sample

For objects with electron densities in the range $\sim 100 - 1,000 \text{ cm}^{-3}$, the line ratio will be fairly close to unity, as can be seen in Figure 1. In this regime, relatively small changes in the line flux can result in large changes to the inferred electron density. Therefore, it is imperative that the doublets used to infer electron densities be free of any contamination from skylines or poor line profile fitting. The [S II] doublet is well separated and the two components are fit separately with single

Gaussian profiles. The [O II] doublet is well-resolved but the two components are blended and must be fit with two Gaussian profiles simultaneously. When fitting the [O II] doublet, we constrain the separation of the centroids of the two components to be within 0.5 \AA of the nominal separation of 2.78 \AA in the rest frame. We also require the widths of the two components to match each other exactly and to be no more than 10% larger than the velocity width inferred from the highest signal-to-noise line in the object's spectrum, typically $\text{H}\alpha$ or $[\text{O III}]\lambda 5007$. This method yields robust fits to [O II] doublets.

We select MOSDEF galaxies in the redshift range $2.0 < z < 2.6$ with $S/N \geq 3$ in [O II] $\lambda\lambda 3726, 3729$ or [S II] $\lambda\lambda 6716, 6731$ which have not been flagged as AGN based on their IR and X-ray properties (Coil et al. 2015). This gives a sample of 97 [O II] doublets and 36 [S II] doublets at $z \sim 2.3$. We visually inspected each of these doublets and removed those with significant skyline contamination or spurious detections. One additional [S II] object with a very high value of $\log([\text{N II}]\lambda 6584/\text{H}\alpha) = -0.11$ indicating a probable AGN was also removed, giving a final density sample of 43 [O II] doublets and 26 [S II] doublets from 61 different targets at $\langle z \rangle = 2.24 \pm 0.12$. This sample spans a range of stellar mass from $10^{8.97} - 10^{11.22} M_\odot$ with a median stellar mass of $10^{10.10} M_\odot$. Of the 61 galaxies, 8 (13%) do not have measured SFRs, of which 3 galaxies do not have wavelength coverage of $\text{H}\beta$, 2 galaxies do not have wavelength coverage of $\text{H}\alpha$, and the remaining 3 galaxies show significant skyline contamination of the $\text{H}\beta$ line. The other 53 objects have SFRs spanning $4.65 - 228 M_\odot/\text{yr}$ with a median SFR of $29.7 M_\odot/\text{yr}$. The density sample has only slightly higher median M_* and SFR than the parent sample of MOSDEF $z \sim 2.3$ star-forming galaxies (Section 2.3) and is still representative of the fairly massive $z \sim 2.3$ star-forming galaxy population. The 8 galaxies without SFR measurements are included in all parts of the analysis for which SFR is not required. Examples of [O II] and [S II] doublets from six different objects in the MOSDEF $z \sim 2.3$ sample are shown in Figure 2, along with fits and inferred line ratios.

We use a local comparison sample from SDSS to investigate evolution in the typical densities of star-forming regions. We select galaxies from SDSS in the redshift range $0.04 < z < 0.1$ to attain a sample that is relatively free of aperture effects and limited to the local universe. We require galaxies to have $S/N \geq 3$ in $\text{H}\beta$, [O II] $\lambda 5007$, $\text{H}\alpha$, [N II] $\lambda 6585$, [S II] $\lambda 6716$, and [S II] $\lambda 6731$. Detections in the first four of these lines are required to reject AGN using the empirical demarcation of Kauffmann et al. (2003). We do not require detection of the [O II] doublet. The SDSS spectra have a spectral resolution of ~ 2000 , corresponding to a resolution element of $\sim 1.9 \text{ \AA}$ at 3727 \AA . This resolution is insufficient to properly resolve and sample the [O II] $\lambda\lambda 3726, 3729$ doublet separated by 2.78 \AA (see Section 3.3). Therefore, we only use the [S II] doublet to probe the electron density in the local comparison sample. The local comparison sample contains 99,291 galaxies with $\langle z \rangle = 0.0678$.

3.3. The consistency of [O II] and [S II] electron densities

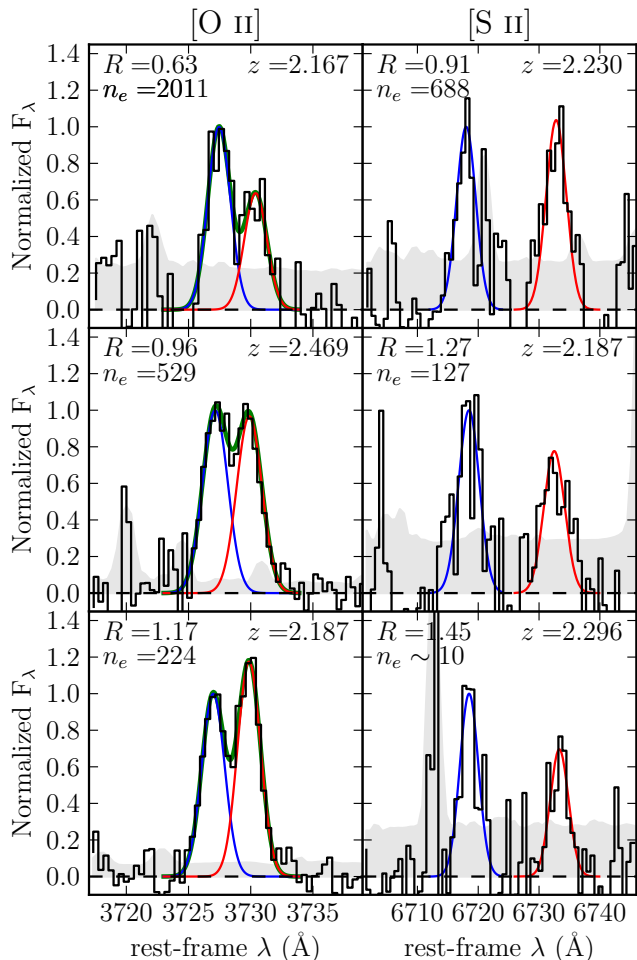


Figure 2. $[\text{O II}]\lambda\lambda 3726, 3729$ doublets (left column) and $[\text{S II}]\lambda\lambda 6716, 6731$ doublets (right column) from six different objects over a range of line ratios and densities. The black line shows the continuum subtracted spectrum for each object. The light gray band indicates the error spectrum for each object, while the blue and red lines show the Gaussian profile fits to the blueward and redward component of each doublet, respectively. The green line shows the total $[\text{O II}]$ profile. In each panel, the spectrum has been normalized so that the blue component has a peak height of unity. The line ratio R , density (n_e) in cm^{-3} , and redshift is displayed for each object, with $R = [\text{O II}]\lambda 3729/\lambda 3726$ in the left column and $R = [\text{S II}]\lambda 6716/\lambda 6731$ in the right column.

Since our high-redshift electron density sample has a mixture of $[\text{O II}]$ and $[\text{S II}]$ doublet measurements while the local comparison sample only has reliable $[\text{S II}]$ measurements, it is a useful exercise to evaluate the consistency of densities determined using these two ionic species to see if they can be directly compared. To this end, we have assembled a sample of local HII regions from the literature with high-resolution, high-signal-to-noise spectroscopic observations with sufficient wavelength coverage to span $[\text{O II}]\lambda\lambda 3726, 3729$ and $[\text{S II}]\lambda\lambda 6716, 6731$. We performed a literature search and identified 32 galactic and extragalactic HII regions observed at high spectral resolution ($R \sim 8,000\text{--}23,000$) with detections of both the $[\text{O II}]$ and $[\text{S II}]$ doublets (García-Rojas et al. 2005, 2006, 2007; López-Sánchez et al. 2007; Esteban et al. 2009, 2013, 2014).

Electron densities and uncertainties are calculated with the same method outlined above using the published line

fluxes and errors. Densities and uncertainties are presented in Figure 3. Four of the 32 individual measurements have $[\text{S II}]\lambda 6716/\lambda 6731$ ratios that are higher than the theoretically allowed maximum in the low-density limit, and thus cannot be assigned a density. While these four objects have $[\text{S II}]\lambda\lambda 6716, 6731$ detected at greater than 3σ indicating they are in the low-density limit, we plot them as upper limits (red squares) where the data point is plotted at the $[\text{S II}]$ density corresponding to the lower 1σ uncertainty on the $[\text{S II}]$ line flux ratio. Fitting a line in logarithmic space yields the relationship

$$\log\left(\frac{[\text{S II}]\ n_e}{\text{cm}^{-3}}\right) = 1.00^{+0.29}_{-0.12} \times \log\left(\frac{[\text{O II}]\ n_e}{\text{cm}^{-3}}\right) - 0.01^{+0.32}_{-0.80} \quad (8)$$

where the 68th percentile confidence intervals are determined by perturbing the data points according to their uncertainties and refitting. This best-fit line is shown in Figure 3 as a solid blue line while the light blue shaded region shows the 68th percentile confidence region around the best-fit line. The relation between electron densities determined by $[\text{O II}]$ and $[\text{S II}]$ is completely consistent with a one-to-one relation (dashed black line). All four objects plotted as upper limits are also consistent with a one-to-one relation within the 1σ uncertainties. There are 8 objects in the $z \sim 2.3$ density sample that have density estimates from both the $[\text{O II}]$ and $[\text{S II}]$ doublets, but the number of galaxies is too small and measurement uncertainties are too large to perform a similar investigation at $z \sim 2.3$. We assume that the relationship between densities of star-forming regions determined using $[\text{S II}]$ and $[\text{O II}]$ does not change with redshift. Thus, we conclude that densities determined from either ionic species in the $z \sim 2.3$ sample can be directly compared with each other and with SDSS density measurements from $[\text{S II}]$ doublets.

For this test, we specifically selected a sample with high S/N and very high spectral resolution so that each component of the doublets was well-detected and the $[\text{O II}]$ doublet was well resolved. We note that repeating this exercise with medium-resolution spectra ($R \sim 1,000\text{--}2,000$) of local HII regions (Peimbert et al. 2012; García-Rojas et al. 2014; Berg et al. 2015) yields a relation in which $[\text{O II}]$ electron densities are systematically overestimated with respect to $[\text{S II}]$ electron densities. This effect is very similar to what is seen in the SDSS sample ($R \sim 2,000$). In order to have at least two resolution elements to sample the separation of the $[\text{O II}]$ doublet components, a spectral resolution of $\Delta\lambda = 1.39\ \text{\AA}$ at $\lambda = 3727\ \text{\AA}$ is needed, corresponding to $R \sim 2,700$. MOSDEF observations adequately sample the $[\text{O II}]$ doublet at $z \sim 2.3$ with $R \sim 3,300$ in the J band.

3.4. Typical electron density at $z \sim 2.3$ and $z \sim 0$

We would like to characterize the typical electron density in star-forming regions of $z \sim 2.3$ galaxies and $z \sim 0$ galaxies. However, given the shape of the function in equation 7 and Figure 1, a fairly symmetric distribution of line ratios leads to a very asymmetric distribution in electron densities. Furthermore, the diagnostic curve translating from line ratio to electron density is insensitive to the electron density at very low and very high densities, asymptotically approaching the theoretical maximum and minimum line ratio, respectively, in

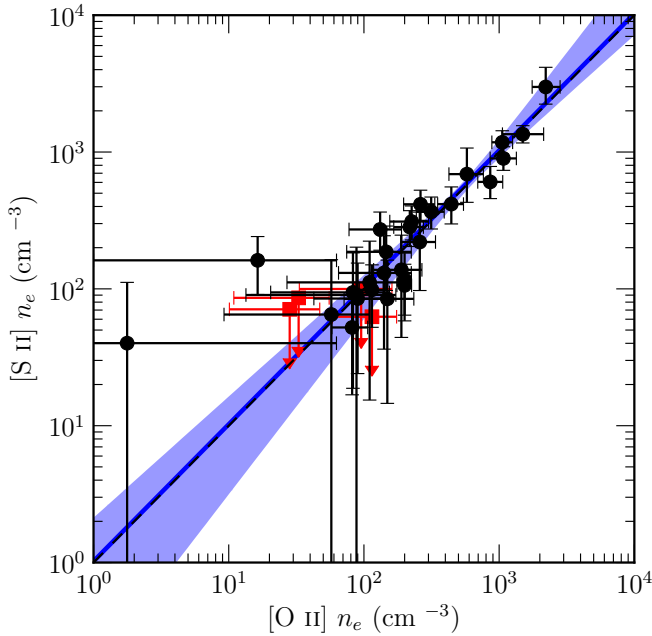


Figure 3. Comparison of density estimates from the [O II] and [S II] doublets for a sample of local HII regions with high-S/N, high-resolution spectra. Black points denote density measurements for individual HII regions. The four red squares show limits plotted at the upper 1σ uncertainty bound on the [S II] density for objects that have higher [S II] λ 6716/ λ 6731 than the maximum theoretically allowed value. The black dashed line shows a one-to-one relationship. The blue line and shaded blue region show the best-fit line and 1σ confidence interval, respectively. Parameters of the best-fit line are shown in equation 8.

those two regimes. Measured line ratios that fall outside of the theoretically allowed region due to measurement uncertainty can only be assigned limits in the low- or high-density extremes. We consider the low-density limit to refer to a density below $\sim 10 \text{ cm}^{-3}$ and the high-density limit to denote density above $\sim 10,000 \text{ cm}^{-3}$. For these reasons, we perform statistics on the line ratio distributions for each sample rather than the electron density distributions and infer typical electron densities based on the statistical properties of the line ratio distribution.

The distributions of line ratios of the $z \sim 2.3$ star-forming galaxies are shown in the top and bottom panels of Figure 4 for the [O II] and [S II] doublets, respectively. We determine the typical electron density from the median line ratio of a given sample. The uncertainty on the median is calculated using a bootstrap technique in which we randomly resample with replacement, perturb the emission line fluxes according to their uncertainties and recalculate the line ratio for each object in the new sample, take the median of the new perturbed sample, and repeat the preceding steps 1,000 times to build up a well-sampled distribution of median values. The reported lower and upper uncertainties on the median are determined to be the 15.8-percentile and 84.2-percentile values, respectively, of the cumulative distribution function of the median. At $z \sim 2.3$, we find a median [O II] λ 3729/ λ 3726 ratio of $1.18^{+0.01}_{-0.10}$ corresponding to an electron density of $225^{+119}_{-4} \text{ cm}^{-3}$. We find a median [S II] λ 6716/ λ 6731 value of $1.13^{+0.16}_{-0.06}$ which gives an electron density of $290^{+88}_{-169} \text{ cm}^{-3}$, consistent within the

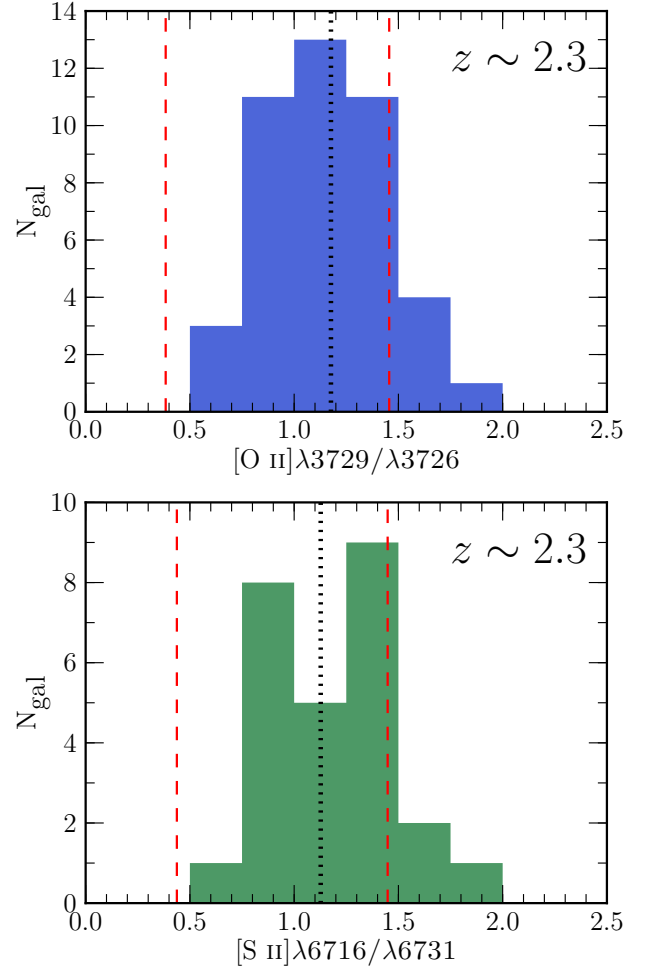


Figure 4. [O II] λ 3729/ λ 3726 (top) and [S II] λ 6716/ λ 6731 (bottom) line ratio distributions for 43 and 26 $z \sim 2.3$ star-forming galaxies, respectively. In each panel, the dotted black line shows the median line ratio (corresponding to an electron density of 225 cm^{-3} for [O II] and 290 cm^{-3} for [S II]), while the dashed red lines show the minimum and maximum theoretically-allowed line ratios from Table 1.

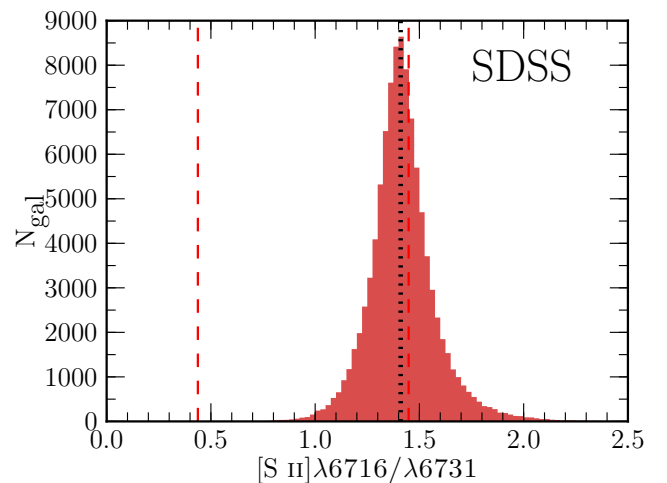


Figure 5. [S II] λ 6716/ λ 6731 line ratio distribution for local star-forming galaxies from SDSS, with lines as in Figure 4. The median line ratio for local galaxies (corresponding to an electron density of 26 cm^{-3}) falls near the low-density limit.

uncertainties with the density determined using [O II]. We measure a range of individual electron densities from the low-density limit to $2,500 \text{ cm}^{-3}$ and find that $z \sim 2.3$ star-forming regions have a typical electron density of $\sim 250 \text{ cm}^{-3}$.

The typical density that we infer for high-redshift galaxies ($\sim 250 \text{ cm}^{-3}$) is in excellent agreement with what Steidel et al. (2014) observed by stacking J-band observations of 113 galaxies at $z \sim 2.3$, finding an average [O II] $\lambda 3729/\lambda 3726$ ratio of 1.16, corresponding to a density of 243 cm^{-3} using the atomic data adopted in this paper. Shimakawa et al. (2015) found a median electron density of 291 cm^{-3} among 14 H α emitters at $z \sim 2.5$ using the [O II] doublet. Previous observations of individual gravitationally lensed galaxies at $z \sim 2$ suggested electron densities of $\sim 1000 \text{ cm}^{-3}$ (Hainline et al. 2009; Bian et al. 2010), somewhat higher than the value we infer. Lehnert et al. (2009) presented electron densities in the range $400 - 1200 \text{ cm}^{-3}$ for 4 galaxies at $z \sim 2.3$ in the SINS survey (Förster Schreiber et al. 2009), also higher than our sample median. As noted in Section 3.1, different choices of atomic data can change the inferred densities by $\sim 30\%$ and can lead to differences of this magnitude in measured densities reported by different authors. In comparison to these previous estimates, except for that of Steidel et al. (2014), our sample is larger and selected in a more systematic way, and the galaxies in our sample display properties representative of the SFR- M_* relation at $z \sim 2$, as shown in Section 2.3. As such, the density estimate presented here should hold true for a population of typical star-forming galaxies at $z \sim 2.3$ with $M_* \gtrsim 10^{9.5} M_\odot$.

For the local comparison sample, we find SDSS star-forming galaxies have a distribution with a median [S II] $\lambda 6716/\lambda 6731$ ratio of 1.41, shown in Figure 5, corresponding to an electron density of 26 cm^{-3} . The uncertainty on the SDSS median line ratio is less than 0.04% due to the large number of galaxies in the sample. We find that the typical electron density in star-forming regions increases by a factor of 10 from $z \sim 0$ to $z \sim 2.3$. The local median [S II] $\lambda 6716/\lambda 6731$ ratio is close to the theoretical maximum ratio of 1.4484, suggesting that local star-forming galaxies typically fall close to the low-density limit. From the slope of the function in Figure 1, it is apparent that the line ratios of both [O II] and [S II] are almost completely insensitive to the density when the electron density is below $\sim 10 \text{ cm}^{-3}$, and are only mildly sensitive to the density below $\sim 50 \text{ cm}^{-3}$. Even if we assume a conservative upper limit of 50 cm^{-3} for the typical local density, we still observe a significant increase in electron density from $z \sim 0$ to $z \sim 2.3$.

The measurements above suggest that $z \sim 2.3$ star-forming regions are typically denser than local star-forming regions by an order of magnitude. We perform some tests to investigate the significance of the observed evolution in electron density. First, note that the SDSS line ratio distribution shown in Figure 5 is well-sampled and fairly narrow. We find that 89% of the SDSS sample has higher [S II] ratios (lower electron densities) than the median $z \sim 2.3$ [S II] ratio, while 64% of the $z \sim 2.3$ sample has lower [S II] ratios (higher electron densities) than the SDSS sample median. A two-sided Kolmogorov-Smirnov test on the $z \sim 0$ and $z \sim 2.3$ [S II] distributions

yields a K-S statistic of 0.452 and a p-value (the probability that the two samples were drawn from the same underlying distribution) of 7.63×10^{-6} , indicating that the $z \sim 0$ and $z \sim 2.3$ density distributions are significantly different.

We are attempting to estimate the electron density in HII regions, but [S II] emission coming from other components of the ISM could contaminate measured [S II] ratios from integrated-light galaxy spectra. The S II ion has an ionization energy of 10.36 eV, somewhat lower than that of hydrogen. Because of its lower ionization energy, the S II zone can extend beyond the boundary of an HII region. Additionally, [S II] $\lambda\lambda 6716, 6731$ emission can be produced in diffuse ionized gas that is shock excited (Reynolds 1985; Martin 1997). To investigate the effects of contamination from a diffuse ionized ISM component, we used measurements of [S II] ratios of 44 HII regions in the star-forming spiral galaxy NGC 628 observed as part of the CHAOS survey (Berg et al. 2015). The spectra of these HII regions were attained by placing slits on top of individual HII regions and should contain very little light from the diffuse ISM. We find that the median [S II] $\lambda 6716/\lambda 6731$ ratio of these HII regions is 1.39, corresponding to an electron density of 38 cm^{-3} . This ratio is nearly equivalent to the median [S II] ratio of 1.41 for the SDSS sample, suggesting that our estimate of the typical local HII region density from SDSS is not significantly biased by emission from diffuse ionized gas. However, all of these HII regions are from a single galaxy, and their median density may not be representative of the entire local HII region population. Currently, there is insufficient knowledge of the ISM structure of $z \sim 2$ galaxies to determine whether integrated-light spectra are significantly contaminated by emission from a diffuse component at that redshift.

3.5. Electron density vs. galaxy properties

We investigate whether the density of star-forming regions varies with other galaxy properties. As stated previously, the nature of the function converting between line ratio and electron density makes it difficult to work with distributions in density space, especially when some objects have measured line ratios that are outside of the theoretically allowed values. For this reason we will look for relationships between density and galaxy properties using the line ratio as a proxy for the density. We plot the line ratios against stellar mass (M_*), star-formation rate (SFR), and specific star-formation rate (sSFR; SFR/M_*) in Figure 6. The middle and right panels of Figure 6 only include the subset of the $z \sim 2.3$ density sample with H α and H β detections. We note that the $z \sim 2.3$ sample has significant overlap with the SDSS sample in M_* , but the two are almost completely disjoint in SFR and sSFR. This difference is consistent with the evolution of the SFR- M_* relation with redshift (Shivaei et al. 2015). We do not see evidence for any significant trends in line ratio (electron density) as a function of stellar mass, SFR, or sSFR among the local SDSS sample or the MOSDEF $z \sim 2.3$ sample. This observation is confirmed by performing a Spearman correlation test on each sample in each parameter space. No correlations are more significant than $\sim 1\sigma$.

This result is in conflict with the recent work of Shimakawa et al. (2015), who found a correlation between

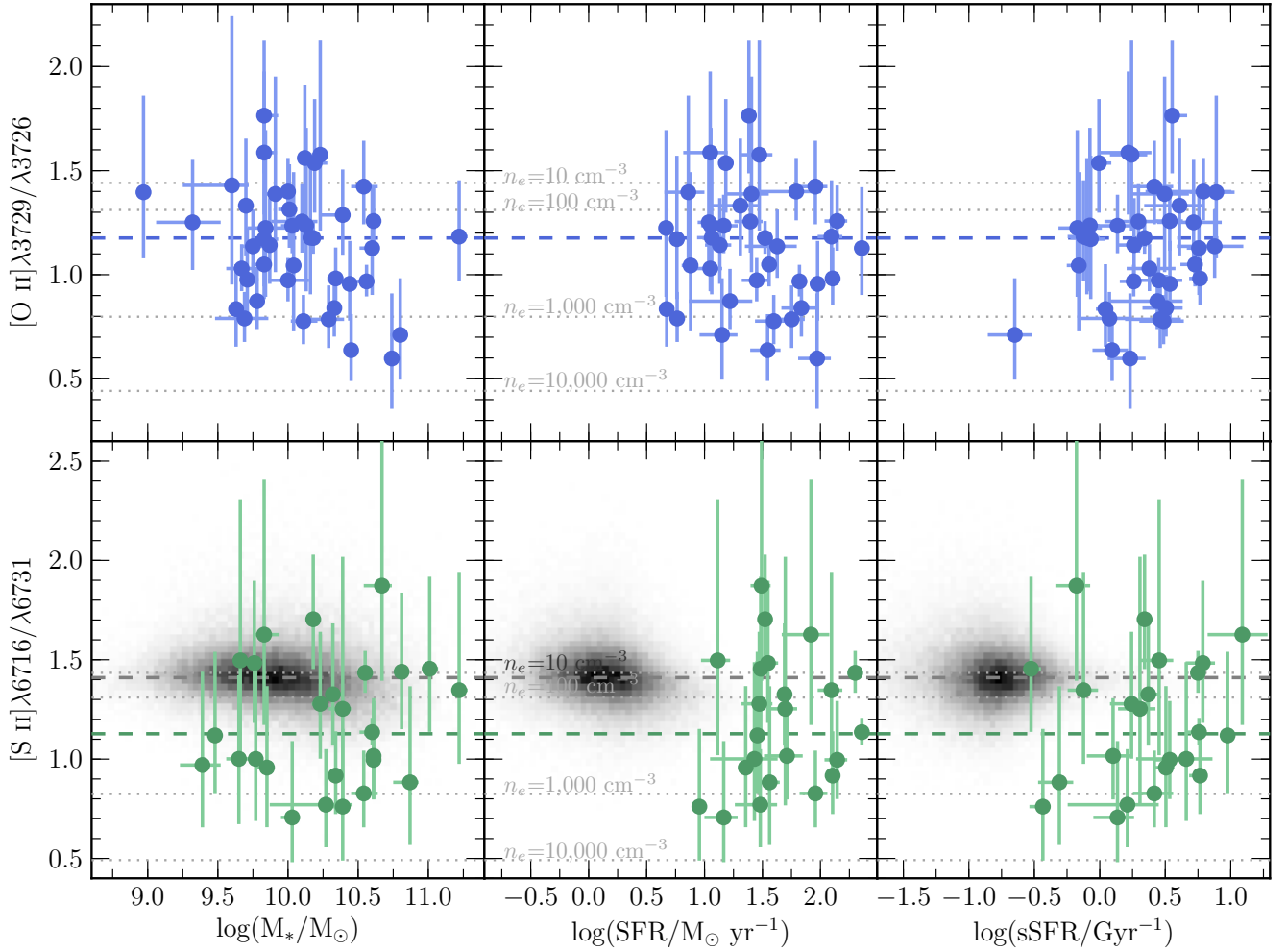


Figure 6. $[\text{S II}]\lambda\lambda 6716, 6731$ (bottom row) and $[\text{O II}]\lambda\lambda 3726, 3729$ (top row) as a function of stellar mass (left), SFR (middle), and sSFR (right). Blue and green points show the $z \sim 2.3$ $[\text{O II}]$ and $[\text{S II}]$ density samples, respectively. The gray two-dimensional histogram in the bottom row shows the distribution of the local comparison sample. Spectra from SDSS do not have a high enough spectral resolution to resolve the components of the $[\text{O II}]$ doublet. The blue, green, and gray dashed lines show the median line ratios for the corresponding densities. Dotted lines show the line ratios corresponding to densities of 10, 100, 1,000, and 10,000 cm^{-3} .

electron density and sSFR at the 4σ level for 14 $z \sim 2.5$ $\text{H}\alpha$ emitters, and observed this correlation when stacking the spectra in two density bins. We do not see evidence for correlation among these properties with a larger and more representative sample that is generally consistent with that of Shimakawa et al. (2015) in stellar mass and SFR. Shimakawa et al. (2015) found no correlation between electron density and stellar mass, in agreement with our results.

4. IONIZATION PARAMETER

The ionization state of ionized gas in star-forming regions refers to the interaction between the ionizing source and ionized gas. This interaction modulates the relative populations of different ionic species, which directly influence the observed emission line ratios. Multiple lines of evidence suggest that the ionization state in high-redshift star-forming regions may be systematically different from what is typically observed in the local universe in galaxies of similar masses (e.g., Holden et al. 2014; Nakajima & Ouchi 2014; Steidel et al. 2014). The ionization parameter is useful for quantifying the ionization state, and

encodes information about both the ionizing source and the surrounding ionized gas. In this section, we will use emission line measurements of $z \sim 2.3$ galaxies to investigate the relationship between ionization parameter and other galaxy properties in order to probe the ionization state of gas in $z \sim 2$ star-forming regions.

4.1. Definition of the ionization parameter

We begin with some useful definitions related to the ionization state. Ionic species in HII regions are in ionization equilibrium, where the rate of ionization is equal to the rate of recombination. The ionization equilibrium condition for ionic species i can be written as

$$n_i \frac{Q_i}{4\pi r^2} \bar{\sigma}_i = n_i^+ n_e \alpha_i \quad (9)$$

where n_i is the number density of the ionic species, Q_i is the rate of production of photons that can ionize species i , $\bar{\sigma}_i$ is the effective ionization cross-section, n_i^+ is the number density of the once-ionized state of n_i , n_e is the electron density, and α_i is the recombination coefficient. If the ionization energy of n_i is close to that of hydro-

gen, which is the case for many of the ions that produce strong optical emission lines, then we can rearrange this expression and approximate the ratio of the relative populations in the higher and lower ionized states.

$$\frac{n_i^+}{n_i} \approx \frac{\bar{\sigma}_i}{\alpha_i} \frac{Q_0}{4\pi r^2 n_e} \quad (10)$$

Here, Q_0 is the rate of production of hydrogen-ionizing photons ($h\nu \geq 13.6$ eV). The first term ($\bar{\sigma}_i/\alpha_i$) on the right hand side of this expression is a constant that will change for each ionic species. The second term ($Q_0/4\pi r^2 n_e$) contains only properties of the ionizing source and the gas, and is not dependent on the specific ionic species. The dimensionless ionization parameter \mathcal{U} is defined as the second term on the right-hand side of equation 10 divided by the speed of light, c .

$$\mathcal{U} = \frac{Q_0}{4\pi r^2 c n_e} \quad (11)$$

Accordingly, the ratio of the relative population in an upper ionization state to that in a lower ionization state scales directly with the ionization parameter. Since the electron density is approximately the hydrogen gas density in a fully-ionized plasma, the ionization parameter can be thought of as the ratio of the number density of hydrogen-ionizing photons to the number density of the hydrogen gas. When working with HII regions it is convenient to define the dimensionless ionization parameter using the radius of a canonical Strömgren sphere, R_S , as the distance between the gas and the ionizing source.

$$\mathcal{U} = \frac{Q_0}{4\pi R_S^2 c n_e} \quad (12)$$

Often, the dimensional ionization parameter, $q = c \times \mathcal{U}$, is used instead, which is the ratio of the flux of ionizing photons at the Strömgren radius to the hydrogen number density. The definition of the Strömgren radius, based on a balance between ionization and recombination rates assuming case B recombination, is

$$R_S = \left(\frac{3Q_0}{4\pi\alpha_B\epsilon n_e^2} \right)^{1/3} \approx \left(\frac{3Q_0}{4\pi\alpha_B\epsilon n_c^2} \right)^{1/3} \quad (13)$$

where ϵ is the volume filling factor of the gas. The volume filling factor can be defined by assuming that the gas is structured in dense clumps that are surrounded by a lower-density medium. In this case, the volume filling factor is defined as

$$\epsilon = \frac{\langle n_e \rangle^2}{n_{e,c}^2} \quad (14)$$

where $\langle n_e \rangle$ is the global average electron density and $n_{e,c}$ is the electron density of the clumps. The volume filling factor is equal to unity for a homogeneous constant-density gas, while its value decreases as the density of the clumps increases relative to the average density. We note that the density estimates from [S II] and [O II] are based on luminosity-weighted measurements of emission line strengths. Since emission strength scales as the square of the density, we are effectively measuring the clump density if a clumpy gas geometry exists, not the global average density (Kennicutt 1984). Using the definition of the Strömgren sphere radius, we can simplify

the ionization parameter and resolve its dependence on only the rate of ionizing photon production, the electron density, and the volume filling factor.

$$\mathcal{U} \propto Q_0^{1/3} n_e^{1/3} \epsilon^{2/3} \quad (15)$$

The ionization parameter has a weak dependence on both the rate of ionizing photon production and the gas density, and is somewhat more sensitive to the volume filling factor, through which this definition of the ionization parameter contains information about the geometry of the gas.

Defining the ionization parameter assuming the geometry of a Strömgren sphere is convenient, but likely does not hold for real HII regions. The Strömgren geometry assumes a sphere of constant density gas that immediately surrounds the central ionizing source. In local HII regions, feedback from stellar winds can clear out a cavity around the ionizing star cluster such that the ionized gas is a shell instead of a filled sphere (e.g., Watson et al. 2008). Accordingly, the Strömgren radius is not necessarily a good representative radius for the separation of the illuminated gas and the ionizing source. It is possible that the wind-blown bubble geometry exists at high redshifts where the intensity of star formation is concentrated, or some entirely different geometry such as intersecting bubbles. The scalings presented in equation 15 should then be used with caution because of the breakdown of the Strömgren approximation. Real HII regions show a variety of complicated substructure and geometry (e.g., Pellegrini et al. 2011). The Strömgren sphere definition of the ionization parameter also assumes that the nebula is radiation-bounded (i.e. no hydrogen-ionizing photons escape) instead of density-bounded (Nakajima & Ouchi 2014), which may not hold true at high redshifts. Additionally, in an integrated spectrum the measured ionization parameter is a luminosity-weighted average of all of the sources of emission inside the aperture, which includes multiple HII regions and emission from other ISM components.

While the ionization parameter carries interesting information about the ionizing source and gas geometry, it can be difficult to determine because it is not directly observable, but can only be estimated using calibrations derived from physically motivated models. The ionization parameter is often estimated using measurements of sets of emission line ratios that have some sensitivity to the ionization state of the gas (e.g., lower- and higher-ionization states), in conjunction with the predictions of a suite of photoionization models (Díaz et al. 2000; Kewley & Dopita 2002; Dors et al. 2011; Levesque & Richardson 2014; Shirazi et al. 2014). Because of differences in the translation between observables and ionization parameter for different photoionization models, it is convenient to instead use an empirical emission line ratio as a proxy for the ionization parameter. Line ratios featuring both higher and lower ionization state transitions from the same element can be used to estimate the ionization parameter because of the relation between the ionization parameter and the relative populations in the two ionization states. Here, we use $O_{32} = [\text{O III}]\lambda\lambda 5007, 4959 / [\text{O II}]\lambda\lambda 3726, 3729$ as a proxy for the ionization parameter. Systematic uncertainties in this approach result from the way in which a given

ionization parameter-sensitive line ratio depends also on the shape of the ionization spectrum and the metallicity of the gas, unless these two properties can be independently constrained.

4.2. Sample selection

In order to study the ionization state of high-redshift galaxies, we selected a sample of star-forming galaxies from the MOSDEF parent spectroscopic sample requiring objects to fall in the redshift range $2.0 < z < 2.6$ and have $S/N \geq 3$ in $[\text{O II}]\lambda\lambda 3726, 3729$, $\text{H}\beta$, $[\text{O III}]\lambda 5007$, and $\text{H}\alpha$. The flux of $[\text{O III}]\lambda 4959$ is taken to be $1/2.98$ of the $[\text{O III}]\lambda 5007$ flux (Storey & Zeippen 2000). $\text{H}\alpha$ and $\text{H}\beta$ detections were necessary in order to correct line fluxes for dust attenuation, which is important for O_{32} because of the large wavelength separation of the emission lines. Objects with $\text{H}\alpha$ and $\text{H}\beta$ detections also have robust dust-corrected SFRs based on $\text{H}\alpha$ luminosities. AGN were identified and removed based on their X-ray and IR properties (Coil et al. 2015) and objects with $[\text{N II}]\lambda 6584$ detected at 3σ or greater were removed if $\log([\text{N II}]\lambda 6584/\text{H}\alpha) > -0.3$. Any AGN not removed by these selection criteria would introduce a bias in emission line ratio diagrams. We discuss reasons why we are confident that our sample does not contain any AGN in Sections 4.4 and 5.4. Six additional objects were removed because of significant skyline contamination in the relevant emission lines. These criteria yield an ionization parameter sample of 103 MOSDEF galaxies and the properties of the sample are shown in Table 2. This sample has properties that are nearly identical to those of the parent MOSDEF spectroscopic sample at $z \sim 2.3$, and is representative of star-forming galaxies with similar stellar masses at this redshift.

In the discussion that follows, we will examine multiple line ratio diagrams, some of which involve additional emission lines along with oxygen and hydrogen Balmer-series strong lines. Therefore, we selected subsamples of the ionization parameter sample that have additional line detection criteria to plot in these spaces. We selected a subsample of 61 galaxies that additionally have $S/N \geq 3$ in $[\text{N II}]\lambda 6585$. We also selected a subset of 53 galaxies with $S/N \geq 3$ in both $[\text{N II}]\lambda 6585$ and $[\text{S II}]\lambda\lambda 6716, 6731$. The sample properties of the $[\text{N II}]$ and $[\text{S II}]$ subsamples are presented in Table 2. These stringent emission line cuts, requiring all or nearly all of the optical strong lines to be detected, introduce a bias against low-mass, low-SFR galaxies. However, the typical galaxy properties of the subsamples are not significantly different from those of the full ionization parameter sample or the MOSDEF parent $z \sim 2.3$ spectroscopic sample. While the $[\text{N II}]$ and $[\text{S II}]$ subsamples have slightly higher M_* and SFR than the full sample, the median values are still consistent with these galaxies falling on or near the $z \sim 2$ SFR- M_* relation (Whitaker et al. 2014; Shivaei et al. 2015).

We select a sample of typical star-forming galaxies in the local universe from SDSS DR7. We require $0.04 < z < 0.1$ and $S/N \geq 3$ in $[\text{O II}]\lambda\lambda 3726, 3729$, $\text{H}\beta$, $[\text{O III}]\lambda 5007$, $\text{H}\alpha$, and $[\text{N II}]\lambda 6585$. Once again, the flux of $[\text{O III}]\lambda 4959$ is assumed to be equal to $1/2.98$ of the $[\text{O III}]\lambda 5007$ flux (Storey & Zeippen 2000). A detection in $[\text{N II}]$ is required because AGN are rejected using the demarcation of Kauffmann et al. (2003) in the $[\text{O III}]/\text{H}\beta$ vs. $[\text{N II}]/\text{H}\alpha$ diagram. These criteria yield a local sam-

ple of 68,453 star-forming galaxies at $z \sim 0.07$. We also selected a subsample of 65,000 local galaxies that additionally have $S/N \geq 3$ in $[\text{S II}]\lambda\lambda 6716, 6731$.

4.3. O_{32} and global galaxy properties

Many studies have suggested that $z \gtrsim 2$ galaxies have systematically higher ionization parameters than are typical for local galaxies (Holden et al. 2014; Nakajima et al. 2013; Nakajima & Ouchi 2014; Shirazi et al. 2014; Steidel et al. 2014). However, it is imperative to consider the evolution in global galaxy properties with redshift when interpreting the apparently high ionization parameters observed at high redshifts. To this end, we investigate the dependence of the ionization parameter on global galaxy properties through the proxy of O_{32} , motivated by the comparisons performed in Nakajima & Ouchi (2014). Figure 7 presents O_{32} vs. SFR and sSFR for local star-forming galaxies (gray histogram) and the $z \sim 2.3$ ionization parameter sample (red circles), while Figure 8 shows the dependence of O_{32} on stellar mass for the same samples. As described in Section 3.5, the $z \sim 2.3$ galaxies span a similar range in M_* as local SDSS galaxies, but have significantly higher SFR and sSFR at a given stellar mass, consistent with the evolution of the SFR- M_* relation with redshift (Reddy et al. 2012; Whitaker et al. 2014; Shivaei et al. 2015).

Figure 7, top panel, shows that there is a weak anti-correlation between O_{32} and SFR for local galaxies, although there is significant scatter in O_{32} at fixed SFR. Performing a Spearman correlation test yields a correlation coefficient of -0.19, indicating a weak anti-correlation, with a p-value⁸ that is essentially zero due to the large sample size from SDSS. It is known that there is an anti-correlation between metallicity and ionization parameter in the local universe (Dopita & Evans 1986; Dopita et al. 2006a,b; Pérez-Montero 2014; Sánchez et al. 2015), while SFR and metallicity are correlated with large scatter (Mannucci et al. 2010; Lara-López et al. 2013). Therefore, SFR and ionization parameter are anti-correlated (with large scatter) and the top panel of Figure 7 confirms that O_{32} acts as a proxy for the ionization parameter. The $z \sim 2.3$ galaxies also show a weak anti-correlation between O_{32} and SFR, with a Spearman correlation coefficient of -0.30 and a p-value of 0.002.

In the bottom panel of Figure 7, there is a tight correlation between sSFR and O_{32} for $z \sim 0$ galaxies, with a Spearman correlation coefficient of 0.42. The bulk of local star-forming galaxies lie on this relation, while a small fraction of local galaxies with the least star formation ($\log(\text{sSFR}) \lesssim -1.0$) do not show any correlation. It is possible that these low-sSFR galaxies have a very low level of ongoing star formation and are transitioning to the red sequence via secular evolution or some other mechanism associated with the cessation of star formation. The ISM conditions in these low-sSFR galaxies may be different from those in typical local star-forming galaxies and would not be expected to follow the same trends. While $z \sim 2.3$ galaxies inhabit much of the same parameter space as highly star-forming local

⁸ In the Spearman correlation test, the p-value represents the probability of the dataset being drawn from an uncorrelated underlying distribution. A correlation or anti-correlation with a p-value less than 0.003 has a significance greater than 3σ .

Table 2
Properties of the full ionization parameter sample, and [N II] and [S II] subsamples

	$\langle z \rangle^a$	σ_z^b	$\log(M_*/M_\odot)^c$	$\log(M_*/M_\odot)_{\text{med}}^d$	SFR ^e	SFR _{med} ^f
Full sample	2.29	0.11	8.97 – 11.22	10.0	1.61 – 228	23.8
[N II] subsample	2.28	0.11	9.3 – 11.22	10.22	4.71 – 228	33.2
[S II] subsample	2.29	0.11	9.3 – 11.22	10.26	5.77 – 228	33.3

^aAverage redshift of galaxies in the sample.

^bStandard deviation of the redshift distribution.

^cRange of $\log(M_*/M_\odot)$ of galaxies in the sample.

^dMedian $\log(M_*/M_\odot)$ of galaxies in the sample.

^eRange of SFR in M_\odot/yr^{-1} of galaxies in the sample, determined from dust-corrected H α luminosity.

^fMedian SFR in M_\odot/yr^{-1} of galaxies in the sample, determined from dust-corrected H α luminosity.

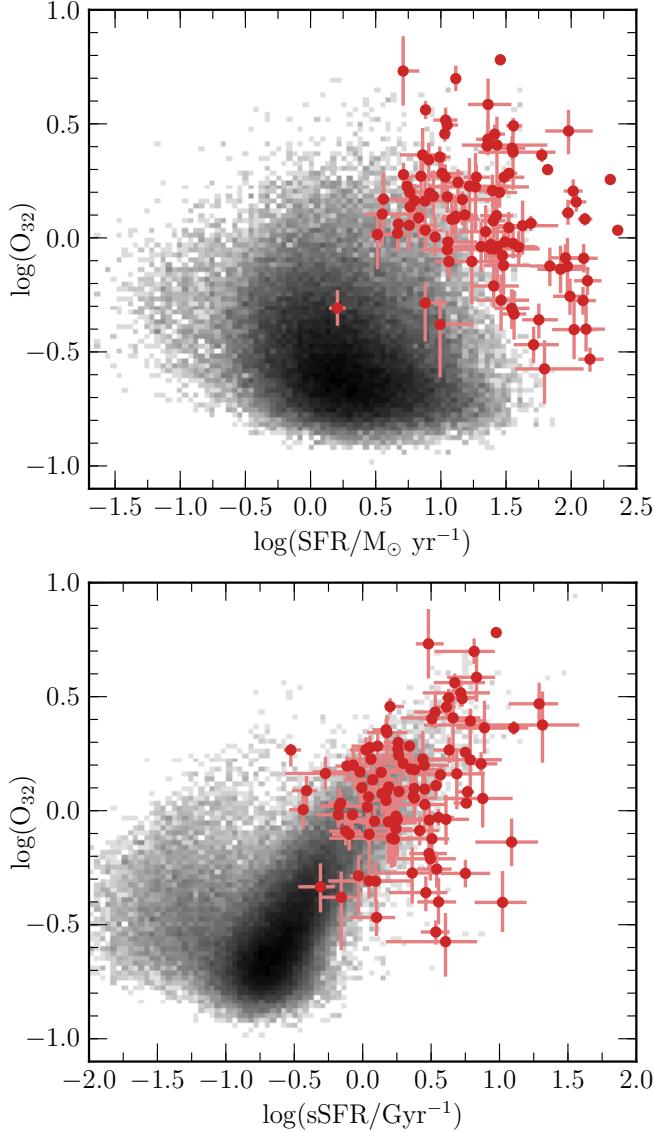


Figure 7. O_{32} vs. SFR (top) and sSFR (bottom) for local star-forming galaxies from SDSS (gray histogram) and $z \sim 2.3$ star-forming galaxies from MOSDEF (red circles).

galaxies, they do not exhibit the same tight correlation between sSFR and O_{32} . Performing a Spearman correlation test yields a correlation coefficient of 0.28 with a p-value of 0.004, indicating a weak but significant correlation. There is significant scatter in O_{32} at fixed sSFR, and a non-negligible fraction of the high-redshift sample

has high sSFR and low O_{32} , a region of the parameter space where essentially no local galaxies are found. The difference between $z \sim 0$ and $z \sim 2.3$ galaxies in this space is interesting, but outside of the scope of this investigation.

The most intriguing of these diagrams is that of O_{32} vs. M_* , shown in Figure 8. Local galaxies show a clear anti-correlation between O_{32} and M_* that is fairly tight, with a Spearman correlation coefficient of -0.52. In order to make the local trend more clear, Figure 8 shows the running median O_{32} at a given M_* as a white line. This anti-correlation is consistent with the existence of a tight correlation between M_* and metallicity, known as the mass-metallicity relation (MZR; Lequeux et al. 1979; Tremonti et al. 2004; Kewley & Ellison 2008; Mannucci et al. 2010; Andrews & Martini 2013), and an anti-correlation between metallicity and ionization parameter (Pérez-Montero 2014; Sánchez et al. 2015). In fact, O_{32} has been shown to be a metallicity indicator for objects up to $z \sim 0.8$ (Maiolino et al. 2008; Jones et al. 2015). The relation between O_{32} and M_* appears to flatten out at high stellar masses, consistent with the observed behavior of the local MZR.

The $z \sim 2.3$ sample also displays a fairly tight relation between O_{32} and M_* such that higher M_* corresponds to lower O_{32} , with a Spearman correlation coefficient of -0.57 and a p-value of 3.7×10^{-10} . We show the running median O_{32} of the high-redshift galaxies at a given M_* as a dark red line in Figure 8. The high-redshift anti-correlation shows nearly the same slope as that of the local relation, only offset towards higher O_{32} at fixed M_* . We find that $z \sim 2.3$ galaxies have O_{32} values ~ 0.6 dex higher at a given M_* , suggesting that high-redshift galaxies have significantly higher ionization parameters than local galaxies of the same stellar mass if the translation between O_{32} and ionization parameter is the same at both redshifts. Stellar mass and metallicity are correlated at $z \sim 2.3$ as well (e.g., Erb et al. 2006; Maiolino et al. 2008; Steidel et al. 2014; Sanders et al. 2015), but the MZR evolves such that galaxies at a given M_* have lower metallicities than are observed locally. The existence of a clear O_{32} vs. M_* anti-correlation at $z \sim 2.3$ is suggestive of an anti-correlation between metallicity and ionization parameter existing at high redshifts as well.

The striking similarity of the shape of the O_{32} vs. M_* relation for local and $z \sim 2.3$ galaxies suggests that a similar mechanism may set the observed ionization parameter at both redshifts, but must evolve with redshift such that high-redshift galaxies have higher ionization parameters at a given stellar mass. The evolution of the

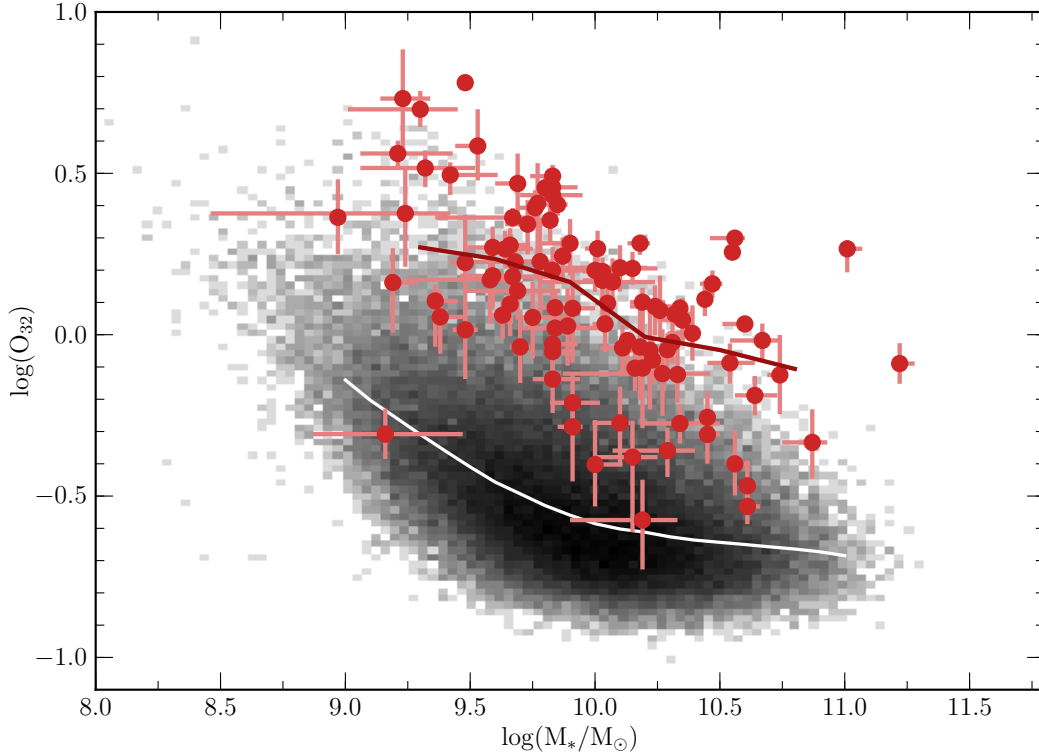


Figure 8. O_{32} vs. stellar mass for local star-forming galaxies from SDSS (gray histogram) and $z \sim 2.3$ star-forming galaxies from MOSDEF (red circles). The solid white line shows the running median O_{32} in bins of stellar mass for local galaxies. The solid dark red line shows the running median of $z \sim 2.3$ galaxies.

MZR from $z \sim 0$ to $z \sim 2.3$ provides a natural explanation for the apparent change in ionization parameter at fixed stellar mass. We further investigate the interplay of O_{32} , M_* , and metallicity by employing the use of emission line ratio diagrams.

4.4. O_{32} and metallicity

We have shown that there is a relation between O_{32} and M_* , the shape of which is similar for local and $z \sim 2.3$ galaxies, that has a higher normalization in O_{32} at high redshift. However, stellar mass is a global property that is not directly related to the production of emission lines in individual star-forming regions that are an observable probe of the ionization parameter. The metallicity of the gas in star-forming regions, on the other hand, has a direct impact on both the ionizing spectrum, assuming the gas-phase metallicity is related to the stellar metallicity of the ionizing cluster, and the intrinsic emission line fluxes. Therefore, comparing O_{32} values at fixed metallicity rather than fixed M_* utilizes a property that directly influences the physical conditions in star-forming regions, including ionization parameter, and removes systematic effects introduced by the evolution of galaxy scaling relations with M_* .

Figure 9 shows the dependence of O_{32} on R_{23} (left) and $O3N2$ (right) for local SDSS galaxies (gray histogram) and the $z \sim 2.3$ ionization parameter sample. Note that the right-hand panel only includes high-redshift galaxies in the $[N\ II]$ subsample since the $O3N2$ ratio requires $[N\ II]\lambda 6584$. Figure 9 demonstrates that the $z \sim 2.3$ sample is likely free from AGN contamination. AGN are found at low $O3N2$, high R_{23} , and high O_{32} . No galaxies in the $z \sim 2.3$ sample fall on the AGN sequence

in the $O3N2$ diagram. In the R_{23} diagram, there are several $z \sim 2.3$ galaxies in the same region of parameter space as the AGN sequence ($\log(R_{23}) > 0.95$), but these galaxies fall below the Kauffmann et al. (2003) line in the $[O\ III]/H\beta$ vs. $[N\ II]/H\alpha$ diagram and tend to have large uncertainties in R_{23} .

The R_{23} index is sensitive to metallicity, but is double-valued (Kewley & Dopita 2002). This problem can be overcome by using a second excitation-sensitive line ratio in tandem with R_{23} . Shapley et al. (2015) used direct-method abundances of stacks of local galaxies (Andrews & Martini 2013) to show that the local sequence in the O_{32} vs. R_{23} diagram is a sequence in monotonically increasing metallicity from the high- O_{32} , high- R_{23} , high-excitation tail towards the low- O_{32} , low- R_{23} , low-excitation region. The $O3N2$ index is also a metallicity indicator, reflecting the fact that the narrow sequence of star-forming galaxies in the BPT diagram is also a sequence in metallicity, and has been used as such in empirical metallicity calibrations (e.g., Pettini & Pagel 2004). The position on either of these diagrams reflects the ionization parameter at a given oxygen abundance.

Using a smaller sample from the early MOSDEF dataset, Shapley et al. (2015) showed that $z \sim 2.3$ star-forming galaxies seem to follow the same distribution as local galaxies in the low-metallicity, high-excitation tail of the O_{32} vs. R_{23} diagram. We confirm this finding with the current MOSDEF $z \sim 2.3$ sample. The $z \sim 2.3$ galaxies display no systematic offset with respect to the local galaxies, and the bulk of the high-redshift sample inhabits the region in which $12 + \log(O/H) \lesssim 8.6$ for local galaxies. The running median of the $z \sim 2.3$ sample (dark red line) closely follows that of $z \sim 0$ galaxies

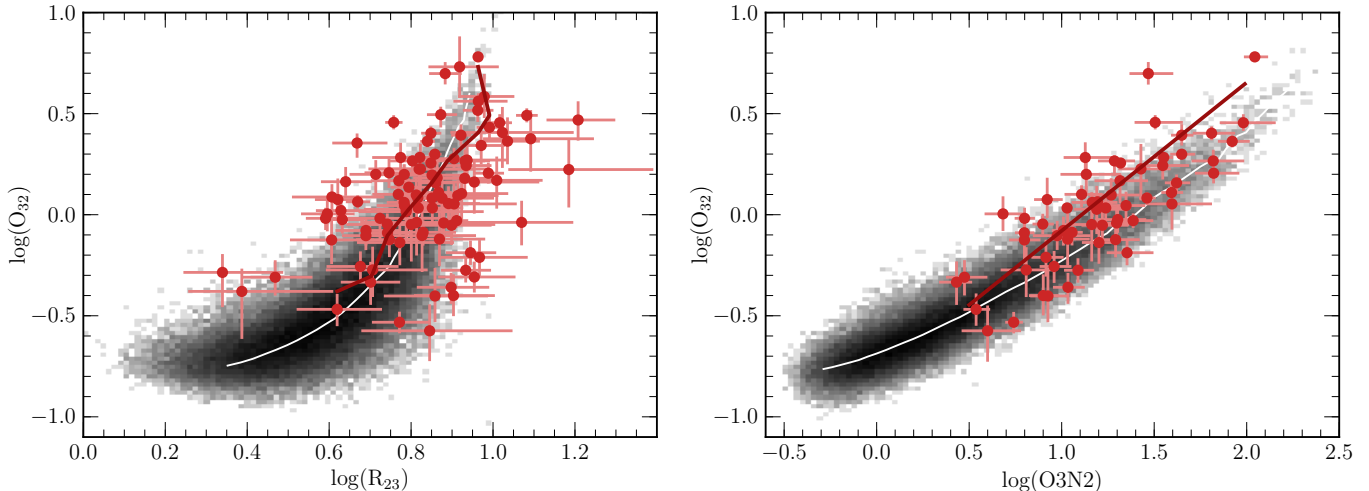


Figure 9. O_{32} vs. R_{23} (left panel) and O_{32} vs. O_{3N2} (right panel). The gray histogram shows the distribution of local star-forming galaxies from SDSS. The red points and error bars denote $z \sim 2.3$ star-forming galaxies from the MOSDEF survey. In both panels, the white line shows the running median of the local sample. The dark red line shows the running median of the $z \sim 2.3$ in the left panel, and the best-fit linear relation to the $z \sim 2.3$ galaxies in the right panel. The right panel only includes galaxies in the [N II] subsample.

(white line) in the O_{32} vs. R_{23} diagram.⁹ We also find that $z \sim 2.3$ galaxies closely follow the subsolar abundance tail of the local distribution in the O_{32} vs. O_{3N2} diagram, although there is a slight systematic offset towards lower O_{3N2} at fixed O_{32} . By comparing the best-fit linear relation of the $z \sim 2.3$ sample (dark red line) to the running median of the $z \sim 0$ sample (white line), we find the mean value of this offset to be 0.23 dex in O_{3N2} at fixed O_{32} . We will discuss the offset in the O_{3N2} diagram further in Section 5.2.

We propose the following scenario to explain the observed position of high-redshift galaxies in the O_{32} vs. R_{23} , O_{32} vs. O_{3N2} , and O_{32} vs. M_* diagrams. Taken together, the two plots in Figure 9 suggest that the ionization parameter at fixed metallicity is the same for galaxies at $z \sim 2.3$ and $z \sim 0$. Galaxies at high redshift must then follow the same anti-correlation between oxygen abundance and ionization parameter that is observed locally. This \mathcal{U} vs. O/H relation shows little to no redshift evolution between $z \sim 0$ and $z \sim 2.3$. The nearly constant offset towards higher O_{32} at fixed M_* observed in Figure 8 is then simply a consequence of the evolution of the MZR with redshift. In Sanders et al. (2015), we found $z \sim 2.3$ galaxies have metallicities ~ 0.3 dex lower than local galaxies at fixed M_* using the O_{3N2} calibration of Pettini & Pagel (2004). If $z \sim 0$ and $z \sim 2.3$ galaxies follow the same metallicity-ionization parameter relation, then the decrease in metallicity at fixed M_* leads to an increase in O_{32} , as observed in Figure 8.

Earlier results suggesting that high-redshift galaxies have higher ionization parameters than are seen locally were based on either a comparison at fixed stellar mass (e.g., Holden et al. 2014) or a comparison of the average ionization parameter of the entire local star-forming pop-

ulation to that of high-redshift galaxies (e.g., Hainline et al. 2009). At fixed metallicity, which is more directly related to the ionization state of the gas, we find that $z \sim 2.3$ galaxies have roughly the same ionization parameters compared to local galaxies. The ionization state of star-forming regions in galaxies in our high-redshift sample must then be similar to what is observed in metal-poor local galaxies.

In Section 3, we found that the density of star-forming regions increases significantly from $z \sim 0$ to $z \sim 2.3$. Here, we are suggesting that galaxies at $z \sim 0$ and $z \sim 2.3$ have the same ionization parameter at fixed metallicity despite the difference in density. This initially seems to be at odds with the scaling of ionization parameter with density presented in equation 15. An increase in density of an order of magnitude would correspond to an increase in the ionization parameter of more than a factor of two. Shirazi et al. (2014) used the relation between ionization parameter and electron density to explain the high ionization parameters observed at $z \sim 2-3$ by an increase in the density of star-forming regions. If the scalings in equation 15 hold at $z \sim 0$ and $z \sim 2.3$, then an increase in density does not guarantee an increase in the ionization parameter unless the volume filling factor is the same at both redshifts. If high-redshift HII regions are clumpier, the volume filling factor would decrease with redshift and could offset the effect of an increase in density. However, the scalings presented in equation 15 are derived assuming the Strömgen approximation, which does not apply to many local HII regions and likely does not hold at $z \sim 2.3$. Thus, an increase of a factor of 10 in density from $z \sim 0$ to $z \sim 2.3$ does not necessitate higher ionization parameters at fixed metallicity.

Our proposed scenario is only valid if some assumptions hold true. A location in O_{32} vs. R_{23} space must correspond to the same metallicity regardless of redshift. The relation between O_{3N2} and metallicity must not evolve significantly with redshift. Finally, the translation between ionization parameter and O_{32} must not evolve significantly from $z \sim 0$ to $z \sim 2.3$. We investigate the validity of these assumptions in the following section.

⁹ A running median creates a smooth representation of the local sequence of star-forming galaxies because of the large number of galaxies in the local sample. The small number of galaxies in the $z \sim 2.3$ sample and subsamples can cause the running median to be uneven and erratic. A linear fit better represents the $z \sim 2.3$ subsample distributions in the O_{3N2} diagram, while a running median is still used in the R_{23} diagram because the O_{32} vs. R_{23} sequence displays curvature.

5. DISCUSSION

In this section, we present evidence in support of our proposed scenario that $z \sim 2.3$ star-forming galaxies have roughly the same ionization parameter as $z \sim 0$ galaxies when comparing at fixed metallicity. In Section 5.1, we investigate whether the translation between O_{32} and ionization parameter evolves with redshift using a set of simple photoionization models in combination with the observed position of $z \sim 2.3$ galaxies in emission line ratio diagnostic diagrams. We explore whether or not there is evidence that the metallicity dependence of R_{23} and $O3N2$ changes significantly from $z \sim 0$ to $z \sim 2.3$ in Section 5.2. In Section 5.3, we discuss additional evidence for the existence of an anti-correlation between O/H and \mathcal{U} and how the existence of this anti-correlation affects the interpretation of photoionization model grids. In Section 5.4, we use our results to explore the cause of the well-known offset of $z \sim 2$ galaxies in the $[N II]$ BPT diagram compared to local galaxies. Finally, we discuss the uncertainty that diffuse ionized gas introduces in the interpretation of emission line ratios from integrated-light galaxy spectra in Section 5.5.

5.1. *Is the ionization parameter- O_{32} relation redshift invariant?*

We first address whether or not the relationship between ionization parameter and O_{32} is the same at $z \sim 0$ and $z \sim 2.3$. We describe the simple photoionization models used for this analysis, discuss the interdependence of the shape of the ionizing spectrum, ionization parameter, and O_{32} , and estimate the typical ionization parameter of $z \sim 2.3$ and local galaxies based on the models.

5.1.1. *Description of the Cloudy photoionization models*

As previously mentioned, the chief difficulty in determining the ionization parameter is that it can only be done with reference to a specific set of photoionization models. The extent to which the value of the estimated ionization parameter can be trusted depends on how well the models represent the observed objects and can produce self-consistent predictions in multiple line ratio spaces. Given the uncertainty of photoionization models both locally and at high-redshift where the physical properties are less constrained, we use a suite of simple photoionization models to understand qualitatively the trends in emission line ratios when changing the different input parameters of the models. We do not, however, use these models to place tight constraints on the metallicity or ionization parameter of any local or high-redshift galaxies.

We use the photoionization code Cloudy¹⁰ to model emission line ratios from star-forming regions with a range of physical conditions. These models are very similar to those used by Steidel et al. (2014) to investigate the position of $z \sim 2.3$ galaxies in the $[O III]/H\beta$ vs. $[N II]/H\alpha$ diagram. There are five main input parameters that determine the location of a grid point in various emission line ratio diagrams: hydrogen gas density, gas-phase metallicity, ionization parameter, shape of the ionizing spectrum, and N/O abundance ratio.

In Section 3, we presented a robust characterization of the typical electron density in local and $z \sim 2.3$ galaxies, finding densities of $\sim 25 \text{ cm}^{-3}$ and $\sim 250 \text{ cm}^{-3}$, respectively. In HII regions, the gas is fully ionized and the electron density provides a good estimate of the hydrogen gas density. Since we have measured the typical density at $z \sim 0$ and $z \sim 2.3$, we only allow the density to be either 25 cm^{-3} or 250 cm^{-3} in the models. The metallicity sets the global abundance scale of the gas, which is assumed to follow a solar abundance pattern with the exception of nitrogen. We vary the metallicity between $0.2 Z_{\odot}$ and $1.0 Z_{\odot}$ ($12 + \log(O/H) = 8.0 - 8.69$) in $0.2 Z_{\odot}$ steps with solar metallicity corresponding to $12 + \log(O/H)_{\odot} = 8.69$ (Asplund et al. 2009). The ionization parameter sets the ionization state of the gas and is allowed to vary between $\log(\mathcal{U}) = -3.6$ and -1.5 ($\log(\frac{q}{\text{cm/s}}) = 6.9 - 9.0$) in 0.1 dex steps.

As described in Section 4.1, the shape of the ionizing spectrum affects the relative populations of an element in different ionized states. A harder ionizing spectrum results in a larger fraction of oxygen in O III compared to O II, for example. We use a blackbody spectrum with an effective temperature of 40,000 K, 50,000 K, or 60,000 K as the input ionizing spectrum. Steidel et al. (2014) showed that, when properly normalized, a blackbody spectrum is a good approximation of the spectrum of massive stars bluewards of 912 Å using BPASS stellar models that include effects from binarity (Eldridge et al. 2011; Eldridge & Stanway 2012). We have found this observation to hold true when using Starburst99 (SB99) stellar models that include effects of rotation in massive stars (Leitherer et al. 2014). We note that the effective temperature of the blackbody is not the same as the effective temperature of a star. It is simply a parameter that allows us to specify the shape of the input spectrum. When referring to a “harder” ionizing spectrum, we are referring to an increase in the blackbody effective temperature of the input spectrum. We additionally utilize input spectra produced by SB99 using the Geneva 2012/13 tracks (Ekström et al. 2012; Georgy et al. 2013) that include the effects of rotation in massive stars (Leitherer et al. 2014). We create two input spectra from SB99 that create bracketing cases of a very hard ionizing spectrum, which we refer to as “*SB99 hard*”, and a softer ionizing spectrum, which we refer to as “*SB99 soft*.” *SB99 hard* is produced assuming a single burst of star-formation that formed 0.5 Myr ago with stellar metallicity of $1/7 Z_{\odot}$. *SB99 soft* instead assumes a 10 Myr-old population with solar metallicity formed with a continuous SFR of $1 M_{\odot}/\text{yr}$. An age of 10 Myr was chosen to ensure that the ionizing spectrum of the stellar population had reached a steady state, occurring after ~ 5 Myr (Kewley et al. 2001). In both cases, a Salpeter (1955) IMF slope is assumed above $0.5 M_{\odot}$. These two cases roughly bracket the range of ionizing spectra appropriate for HII regions contributing significantly to integrated-light galaxy spectra.

In reality, the shape of the ionizing spectrum should be related to the gas-phase metallicity, which traces the stellar metallicity since recently formed massive stars are ionizing the remnants of their birth cloud. In lower metallicity stars, there is less metal line blanketing and opacity in the stellar atmospheres, leading to hotter ef-

¹⁰ Calculations were performed with version 13.02 of Cloudy, last described by Ferland et al. (2013).

fective temperatures and harder ionizing spectra. However, we allow the shape of the ionizing spectrum to vary separately from the metallicity to accommodate the possibility that the hardness of the ionizing spectrum at fixed metallicity evolves with redshift.

A solar abundance pattern is assumed for all elements except nitrogen. In the local universe, the N/O abundance ratio is observed to have a dependence on O/H, such that N/O is a constant value at low abundance but begins to rise roughly linearly with O/H at higher abundance (Pérez-Montero & Contini 2009; Pilyugin et al. 2012; Andrews & Martini 2013; Pérez-Montero 2014). At low metallicity, nitrogen is a primary nucleosynthetic product of hydrogen and helium burning. At high metallicity, nitrogen is produced as a secondary product through the CNO cycle where the yield of nitrogen depends on the amount of pre-existing C and O, which leads to the dependence of N/O on O/H (van Zee & Haynes 2006). There is disagreement about the shape of the N/O vs. O/H relation (see Fig. 12 in Steidel et al. 2014). We assume the relation found by Pérez-Montero & Contini (2009), which is a simple linear relation over the range of metallicities considered in the models. We note that the assumed N/O ratio can strongly affect those line ratios involving [N II] λ 6584, but has negligible effects on other line ratios.

5.1.2. Ionization parameter and the hardness of the ionizing spectrum at $z \sim 0$ to $z \sim 2.3$

From the set of models with density, gas-phase metallicity, ionization parameter, ionizing spectrum, and N/O ratio defined as above, we extract the relationship between O_{32} and ionization parameter to resolve its dependence on the various input parameters. Figure 10 shows O_{32} vs. $\log(\mathcal{U})$ for models with electron density of 25 cm^{-3} (top panel) and 250 cm^{-3} (bottom panel). The line color denotes the input spectrum, while the different lines of a single color connect grid points with the same metallicity. We note that the *SB99 hard* models behave very similarly to the 60,000 K blackbody models. The *SB99 soft* spectrum appears to be slightly softer than a 50,000 K blackbody based on the position of the model grids. Variation in N/O has no effect on the relationship between O_{32} and \mathcal{U} . In addition, Figure 10 shows that this relation has very little dependence on the gas density. Lines of constant metallicity show that the relation between O_{32} and \mathcal{U} has only a small dependence on gas-phase metallicity *when the shape of the input spectrum is fixed*. The one exception is for a soft ionizing spectrum with high ionization parameter and low gas density ($T_{\text{eff}} = 40,000 \text{ K}$, $\log(\mathcal{U}) > -2.5$, $n_e = 25 \text{ cm}^{-3}$), a region in which real objects are unlikely to be found. Calibrations of O_{32} and the ionization parameter typically show significant dependence on metallicity because the ionizing spectrum is tied to the metallicity (e.g., Kewley & Dopita 2002). On the other hand, the hardness of the ionizing spectrum has a significant effect on the O_{32} vs. $\log(\mathcal{U})$ relation, such that a harder ionizing spectrum produces a larger O_{32} value at fixed ionization parameter. Therefore, the translation between O_{32} and ionization parameter will only show significant evolution if the hardness of the ionizing spectrum at a given metallicity evolves with redshift.

We investigate the possibility of the shape of the ion-

izing spectrum evolving with redshift by combining the observed line ratios for our $z \sim 2.3$ sample with grids from the Cloudy models in emission line ratio diagrams. It has been proposed that the position of high-redshift galaxies in the [O III]/H β vs. [N II]/H α diagram can be explained by a systematically harder ionizing spectrum compared to that of local galaxies with similar metallicity (Kewley et al. 2013a; Steidel et al. 2014). If true, this explanation would lead to evolution of the ionization parameter- O_{32} relation.

Figure 11 shows the [O III]/H β vs. [N II]/H α ([N II] BPT) diagram (left column) and the [O III]/H β vs. [S II]/H α ([S II] BPT) diagram (right column). The local distribution of star-forming galaxies is shown as the gray histogram in all panels. The top row presents the observed line ratios for the $z \sim 2.3$ [N II] subsample (top left) and [S II] subsample (top right). The middle and bottom rows show the Cloudy model grid points as circles. The size of the circle indicates the metallicity, with the largest size indicating solar metallicity and the smallest size indicating $0.2 Z_{\odot}$. The color indicates the input ionizing spectrum, with the effective temperature listed for blackbodies in the middle row and the bracketing SB99 models shown in the bottom row. Solid lines connect points of constant ionization parameter, with ionization parameter increasing to the upper left. The model grids are only shown for a density of 250 cm^{-3} . Displaying models at a single density will suffice since we are only interested in discerning trends in line ratio with the model input parameters instead of making quantitative predictions. While the absolute line ratios change, the trends with metallicity, ionization parameter, and hardness of the ionizing spectrum are the same regardless of the assumed density. Qualitatively, increasing the electron density while keeping all other parameters fixed increases [O III]/H β , [N II]/H α , and [S II]/H α .

In the top right panel of Figure 11, we observe the well-documented offset of $z \sim 2.3$ galaxies towards higher [O III]/H β and/or [N II]/H α compared to the local star-forming sequence. The magnitude of this offset can be observed by comparing the running median of the $z \sim 2.3$ sample (dark red line) to that of the $z \sim 0$ sample (white line). However, we do not observe a significant offset between $z \sim 0$ and $z \sim 2.3$ galaxies in the [S II] BPT diagram (top left panel), in agreement with results from early MOSDEF data (Shapley et al. 2015). Masters et al. (2014) found a similar result using a composite spectrum of 24 $z \sim 2$ emission-line galaxies from the WISP survey. In the [S II] BPT diagram, the running median of the $z \sim 2.3$ sample is marginally offset to lower [O III]/H β and/or [S II]/H α , although this offset is not significant given the sample size and measurement uncertainty. In the middle and lower left panels, it can be seen that an increase in the hardness of the ionizing spectrum generally moves grid points to higher [O III]/H β and [N II]/H α at fixed metallicity and ionization parameter, which could potentially explain the $z \sim 2.3$ offset. In the [S II] BPT diagram (middle and lower right), the models show that an increase in the hardness of the ionizing spectrum increases [O III]/H β at fixed [S II]/H α . We emphasize that we are using these models to demonstrate how predicted line ratios change qualitatively as the hardness of the ionizing spectrum varies. We are less concerned with a match between a specific blackbody or SB99 spectrum

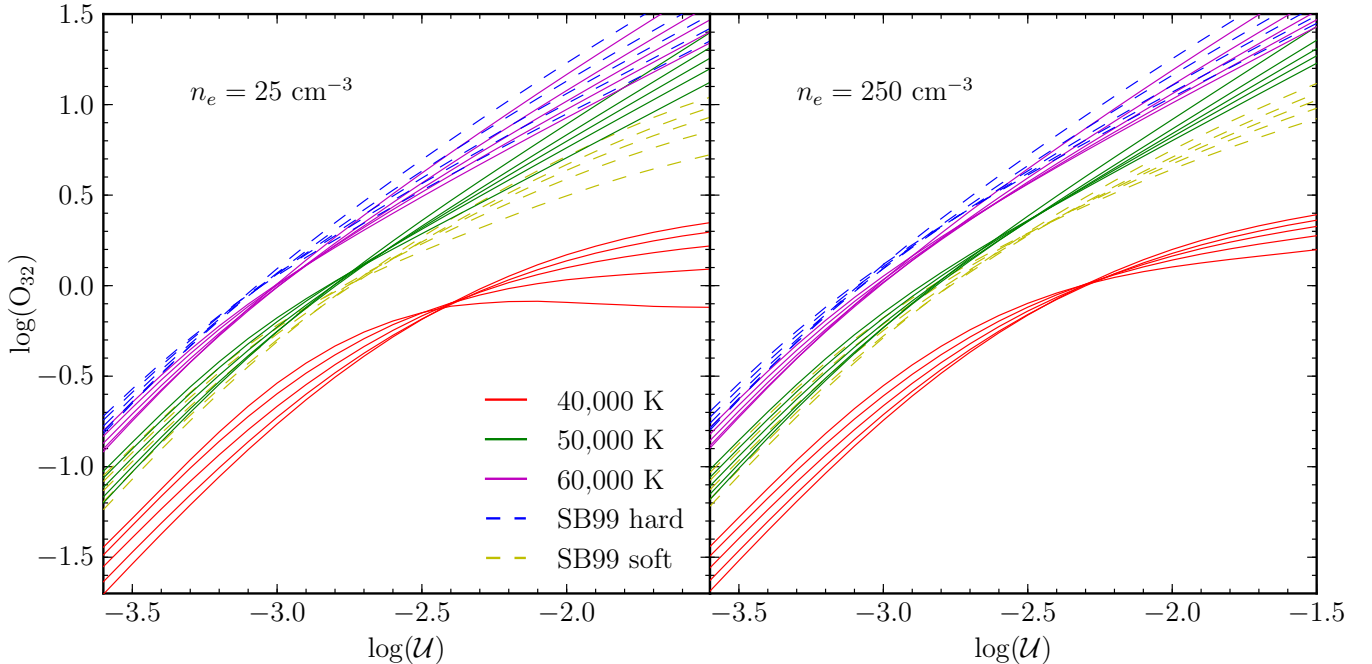


Figure 10. O_{32} vs. ionization parameter, \mathcal{U} , from simple photoionization models of HII regions assuming a gas density of 25 cm^{-3} (top panel) and 250 cm^{-3} (bottom panel). The dependence of O_{32} on \mathcal{U} is extracted from a set of models assuming different ionizing spectra, denoted by the color of the line, and different gas-phase metallicities. Input ionizing spectra are assumed to be either a blackbody spectrum with an effective temperature of 40,000-60,000 K or one of two spectra produced by Starburst99 (*SB99 hard* and *SB99 soft*). Each line of a single color connects models with the same gas-phase metallicity, from $0.2 Z_{\odot}$ to $1.0 Z_{\odot}$.

and either the local or high-redshift excitation sequences.

In both BPT diagrams, an increase in the hardness of the ionizing spectrum leads to a significant increase in $[\text{O III}]/\text{H}\beta$ at fixed $[\text{N II}]/\text{H}\alpha$ or $[\text{S II}]/\text{H}\alpha$ for the same ionization parameter and metallicity. If a harder ionizing spectrum was the cause of the offset of high-redshift galaxies in the $[\text{N II}]$ BPT diagram, simple photoionization models predict that there should also be an offset of similar magnitude towards higher $[\text{O III}]/\text{H}\beta$ in the $[\text{S II}]$ BPT diagram. We observe no significant offset between the $z \sim 2.3$ and $z \sim 0$ galaxies in the $[\text{S II}]$ BPT diagram. We note that in the $[\text{N II}]$ BPT diagram, the 60,000 K and 50,000 K blackbody models approximately match the position of the $z \sim 2.3$ and local galaxies, respectively. The same 60,000 K and 50,000 K blackbody models are offset from one another in the $[\text{S II}]$ BPT diagram, and yet no offset is observed in the corresponding observations of $z \sim 2.3$ and local galaxies. We conclude that there is not a systematically harder ionizing spectrum in high-redshift star-forming regions compared to local star-forming regions of similar metallicity. We will revisit the cause of the $[\text{N II}]$ BPT diagram offset in Section 5.4. Having established that the relation between ionization parameter and O_{32} is only significantly sensitive to changes in the hardness of the ionizing spectrum, we further conclude that the \mathcal{U} - O_{32} relation does not strongly evolve with redshift.

5.1.3. Estimating the typical ionization parameter at $z \sim 2.3$

Having shown that the translation between O_{32} and ionization parameter does not appear to evolve significantly with redshift, we will now estimate the range of ionization parameters that would be inferred from the local and $z \sim 2.3$ galaxy samples. We advise caution when

using these ionization parameter estimates because a different ionizing spectrum should be used for the low- and high-metallicity galaxy populations and the use of different stellar models will change these estimates. Matching the appropriate stellar models to a given object is further complicated by uncertainty in the metallicity estimates used to tie the observed metallicity to the absolute metallicity built into the stellar models. Since we do not know which input ionizing spectrum is appropriate for each sample, we provide estimates of the ionization parameter assuming each of the five ionizing spectra considered in the models. The median $\log(O_{32})$ value of the $z \sim 2.3$ sample is 0.10 and the middle 68% span $\log(O_{32}) = -0.11$ to 0.37. The local SDSS sample has a median $\log(O_{32})$ value of -0.53 and the middle 68% span $\log(O_{32}) = -0.71$ to -0.24 . Estimates of the corresponding values of $\log(\mathcal{U})$ are presented in Table 3 using the curves in Figure 10. We note that the median ionization parameter is approximately the same for $z \sim 0$ and $z \sim 2.3$ galaxies if the ionizing spectrum of local galaxies is well-described by a 40,000 K blackbody and that of $z \sim 2.3$ galaxies is described by a 60,000 K blackbody. However, we have shown that $z \sim 0$ and $z \sim 2.3$ galaxies have similar ionizing spectra at fixed metallicity. While the ionizing spectrum at the median metallicity of each sample will be different, it is unlikely that the magnitude of that difference is as large as the difference between a 40,000 K and 60,000 K blackbody spectrum. Therefore, $z \sim 2.3$ galaxies have a higher median ionization parameter than local galaxies.

5.2. Is the dependence of R_{23} and $O3N2$ on metallicity redshift invariant?

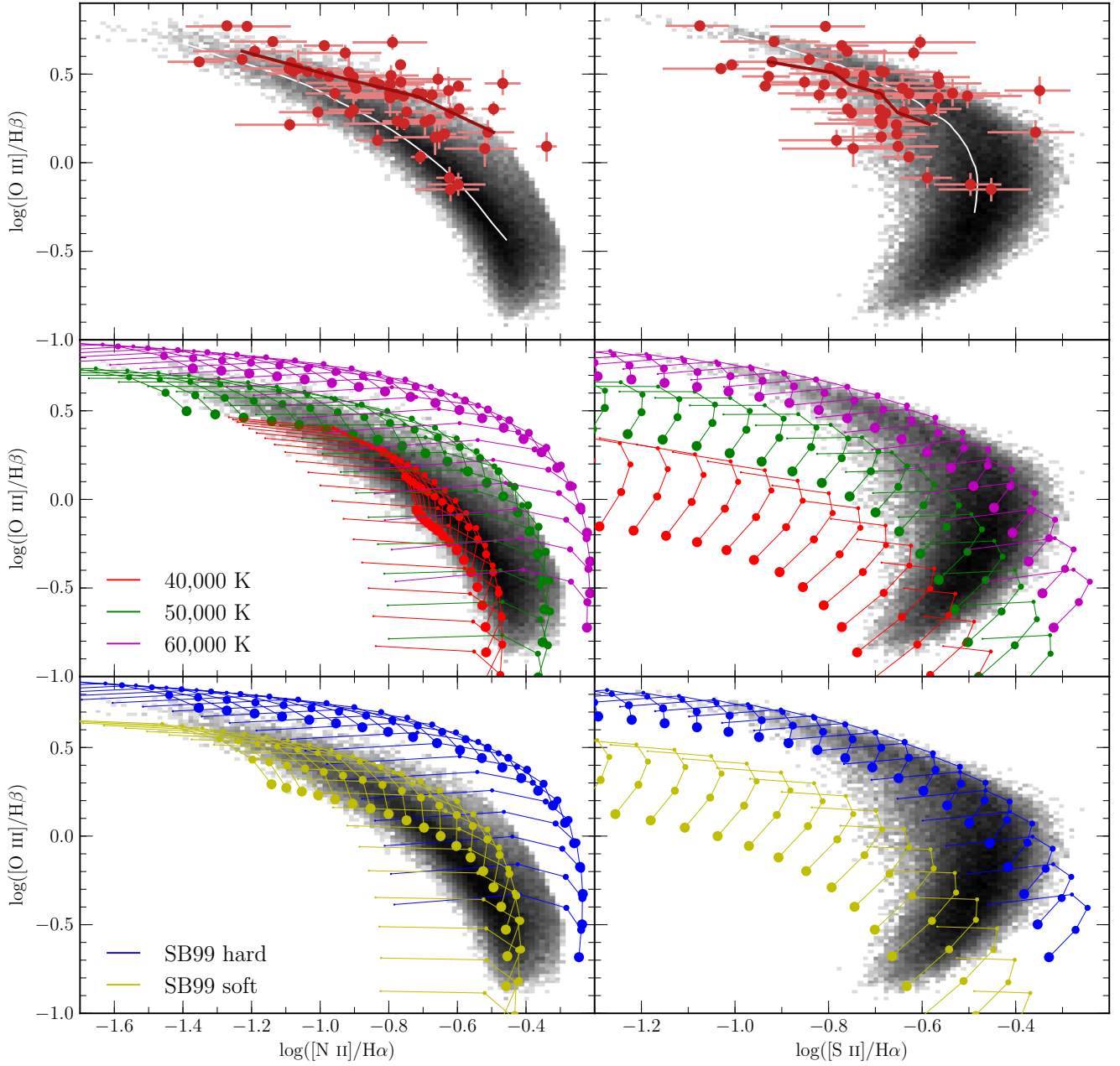


Figure 11. $[\text{N II}]$ (left column) and $[\text{S II}]$ (right column) BPT diagrams. The local sequence of star-forming galaxies from SDSS is shown as the gray histogram in all panels. The top row shows the position of $z \sim 2.3$ star-forming galaxies in the $[\text{N II}]$ and $[\text{S II}]$ BPT diagrams as red points with error bars. The white and dark red lines show the running median of the local and $z \sim 2.3$ samples, respectively. The bottom two rows show grids from simple photoionization models of HII regions produced using Cloudy. Different colors represent different input ionizing spectra. In the middle row, the input ionizing spectrum is assumed to be a blackbody spectrum and the effective temperature is listed, representing the hardness of the ionizing spectrum. In the bottom row, the input ionizing spectrum is assumed to be one of two spectra produced by the stellar population synthesis code Starburst99 (*SB99 hard* and *SB99 soft*). Colored circles show the model grid points, where the size of the circle represents the gas-phase metallicity, from $0.2 Z_{\odot}$ (smallest circles) to solar metallicity (largest circles). Grid points of constant ionization parameter with the same input ionizing spectrum are connected with solid lines. All model grids shown are calculated assuming a hydrogen gas density of 250 cm^{-3} .

Table 3

Ionization parameter estimates of local SDSS and $z \sim 2.3$ star-forming galaxies based on O_{32} for each of the five input ionizing spectra assumed in our photoionization models.

	$\log(O_{32})$		$\log(\mathcal{U})$ assuming an ionizing spectrum of:				
			40,000 K	50,000 K	60,000 K	SB99 soft	SB99 hard
SDSS	median	-0.53	-2.90	-3.20	-3.40	-3.20	-3.45
	lower 68% ^a	-0.71	-3.05	-3.35	-3.50	-3.35	-3.60
	upper 68% ^b	-0.24	-2.60	-3.05	-3.20	-3.00	-3.25
$z \sim 2.3$	median	0.10	-2.10	-2.75	-2.95	-2.70	-3.00
	lower 68% ^a	-0.11	-2.45	-2.95	-3.10	-2.90	-3.15
	upper 68% ^b	0.37	$\gtrsim -1.5^c$	-2.50	-2.70	-2.40	-2.75

^aThe lower bound on the middle 68% of the distribution of $\log(O_{32})$

^bThe upper bound on the middle 68% of the distribution of $\log(O_{32})$

^cThe range of ionization parameters considered in this set of models did not extend high enough to give $\log(O_{32}) = 0.37$ for a 40,000 K blackbody input spectrum, so a lower limit is assigned.

We proposed that the relationship between metallicity and ionization parameter is the same locally and at $z \sim 2.3$. In Figures 10 and 11, we have shown evidence that the relationship between ionization parameter and O_{32} does not significantly change with redshift. In order for the proposed scenario to hold in concordance with Figure 9, we must also show that the dependence of R_{23} and $O3N2$ on metallicity does not significantly evolve with redshift. In Figure 12, we show the local star-forming sample (gray histogram) and the $z \sim 2.3$ $[N II]$ subsample (red circles) in the spaces of O_{32} vs. R_{23} (left), $O3N2$ (middle), and $N2$ (right).

As previously mentioned, no systematic offset is observed between $z \sim 0$ and $z \sim 2.3$ galaxies in the O_{32} vs. R_{23} diagram, although $z \sim 2.3$ objects only occupy the low-metallicity tail of the local distribution. We also pointed out the 0.23 dex offset $z \sim 2.3$ galaxies show towards low $O3N2$ at fixed O_{32} in Section 4.4. We find a larger systematic offset between local and high-redshift galaxies in the O_{32} vs. $N2$ diagram of 0.33 dex higher $N2$ at fixed O_{32} . There is an asymmetric scatter towards high $N2$, such that no $z \sim 2.3$ galaxies scatter below the local sequence. We additionally observed no significant offset in the $[S II]$ BPT diagram (Fig. 11). These results collectively suggest that, on average, high-redshift galaxies have higher $[N II]\lambda 6584$ flux compared to the strength of other strong optical emission lines than typical local galaxies with the same ionization parameter. Outside of line ratios involving nitrogen, high-redshift galaxies appear to behave similarly to the low-metallicity tail of the local distribution. We have measurements constraining the evolution of density with redshift, and have found no evidence suggesting the ionization parameter or hardness of the ionizing spectrum evolve significantly at fixed metallicity. Therefore, we conclude that metallicity indicators involving nitrogen will evolve with redshift, but the relation between metallicity and location in the O_{32} vs. R_{23} diagram is likely the same at $z \sim 0$ and $z \sim 2.3$. Jones et al. (2015) recently found that the relationship between R_{23} , O_{32} , and direct-method metallicity does not evolve out to $z \sim 0.8$. Liu et al. (2008) and Steidel et al. (2014) concluded that the $N2$ indicator significantly over-estimates the metallicity of objects offset from the local star-forming sequence, while the $O3N2$ indicator has a much smaller bias. In conjunction with the arguments presented in Section 5.1, these results support our proposed scenario that galaxies at fixed metallicity have the same ionization parameter locally and at $z \sim 2.3$.

5.3. Additional evidence for the existence of the metallicity-ionization parameter anti-correlation

The argument for an anti-correlation between O/H and ionization parameter arises from the fact that low-metallicity stars produce more ionizing photons in total and have harder ionizing spectrum (Leitherer et al. 2014). Observational evidence for this anti-correlation comes from finding that O_{32} and $[O III]/H\beta$ increase with decreasing metallicity (Maiolino et al. 2008; Jones et al. 2015). However, in Figure 10 it can be seen that harder ionizing spectra give higher values of O_{32} at fixed ionization parameter. We must then consider the possibility that high- and low-metallicity star-forming regions have similar ionization parameters while having higher O_{32} values because of the change in the hardness of the ion-

izing spectrum with metallicity. At fixed \mathcal{U} , the range of ionizing spectra considered in the models spans ~ 0.9 dex in O_{32} . Local star-forming galaxies from SDSS span a range of ~ 1.9 dex in O_{32} from $\log(O_{32}) \sim -1.0$ to 0.9 (see Fig. 9). Based on physically-motivated input spectra, it is not possible for the models to span a range that large in O_{32} at fixed \mathcal{U} . It would require spectra that are harder or softer than what is reasonably expected from models of the young stellar populations responsible for ionizing HII regions. Because the hardness of the ionizing spectrum increases with decreasing metallicity and low-metallicity objects are observed to have higher O_{32} values on average, the only way to produce the dynamic range in O_{32} observed among the SDSS sample is for high-metallicity objects to have low ionization parameters, and vice versa. The relation between O/H and ionization parameter must exist in the local universe, along with a changing ionizing spectrum with metallicity, to reproduce the observed range in O_{32} .

Once established, the existence of an anti-correlation between O/H and ionization parameter lends insight into the interpretation of the simple models presented in Figure 11. Using similar photoionization models to those presented above, Steidel et al. (2014) argued that the sequence of galaxies in the $[N II]$ BPT diagram at low or high redshift is primarily a sequence in ionization parameter because increasing ionization parameter with all other inputs fixed moves grid points along the star-forming sequence. Given the dependence of the ionization parameter and hardness of the ionizing spectrum on O/H , many of the grid points shown in Figure 11 are not descriptions of real objects. We do not expect to see galaxies with high metallicities, high ionization parameters, and hard ionizing spectra. Likewise, galaxies with low metallicities, low ionization parameters, and soft ionizing spectra are not likely to be observed. In fact, it has been previously observed that local HII regions and star-forming galaxies only occupy a narrow subset of the parameter space in photoionization model grids (e.g., Dopita & Evans 1986; Dopita et al. 2006a,b). While individual HII regions can simultaneously demonstrate low metallicity and low ionization parameter, as in the sample discussed in van Zee & Haynes (2006), such objects would contribute negligibly to a luminosity-weighted galaxy-averaged spectrum for galaxies that are actively star-forming.

The star-forming sequence in the $[N II]$ BPT diagram can be understood as a sequence in both ionization parameter and metallicity because the two are fundamentally linked (Bresolin et al. 2012; Sánchez et al. 2015). Steidel et al. (2014) did mention the relations between ionization parameter, metallicity, and ionizing spectrum as a way to reconcile the utility of strong-line metallicity indicators in the *local universe* with the apparent lack of dependence of the star-forming sequence on metallicity in photoionization models. Our results suggest that these relations hold in similar form at $z \sim 2.3$ as well. We note that these relations are traced by the *typical* properties of the galaxy population, and do not preclude the existence of a small number of galaxies in unexpected regions of the parameter space due to scatter in the relations or significantly different conditions caused by some rare process or event, such as a major merger.

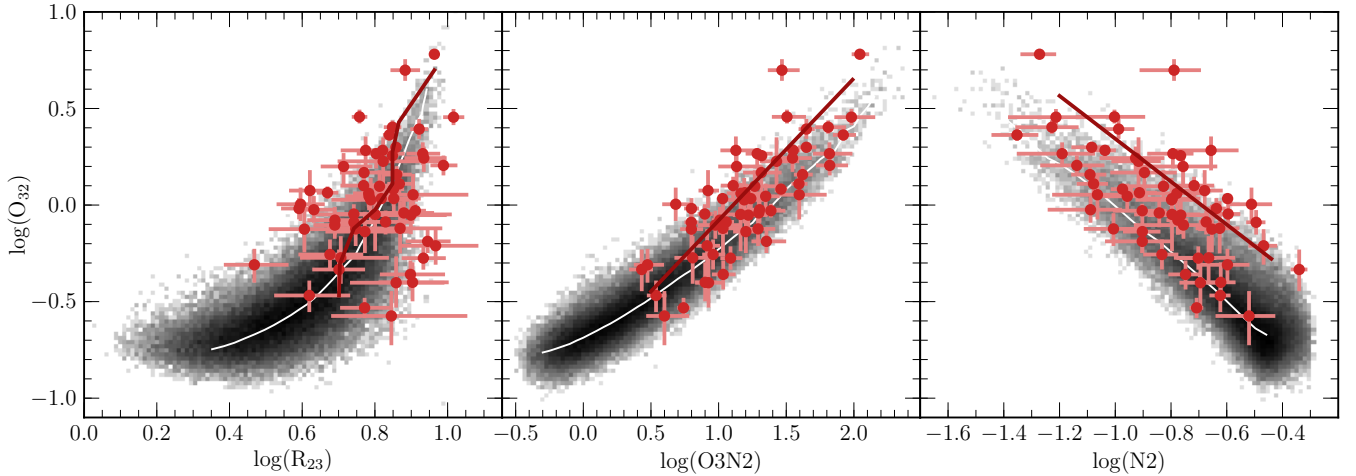


Figure 12. O_{32} vs. R_{23} (left), $O3N2$ (middle) and $N2$ (right) for local star-forming galaxies (gray histogram) and the $z \sim 2.3$ $[N II]$ subsample (red points). In all panels, the white line shows the running median of the local sequence of star-forming galaxies. The dark red line shows the running median of the $z \sim 2.3$ sample in the left panel, and the best-fit linear relation in the middle and right panels.

5.4. Nitrogen abundance and the cause of the $[N II]$ BPT diagram offset

A significant amount of effort has been put forth to find the cause of the offset high-redshift galaxies display in the $[N II]$ BPT diagram (Kewley et al. 2013a,b; Masters et al. 2014; Steidel et al. 2014; Shapley et al. 2015). Proposed causes include systematically higher ionization parameters (Brinchmann et al. 2008), systematically harder ionizing spectra (Steidel et al. 2014), elevated nitrogen abundance at fixed metallicity (Masters et al. 2014; Shapley et al. 2015), and higher gas density/ISM pressure (Kewley et al. 2013a). It has additionally been proposed that the offset in the BPT diagram is an artifact arising from widespread, weak AGN in the high-redshift galaxy population (Wright et al. 2010). Coil et al. (2015) have shown that such global AGN contamination does not appear to be present among $z \sim 2.3$ galaxies from the MOSDEF survey.

In this paper, we have sought to characterize the physical properties influencing the ionization state of high-redshift galaxies, and can now use the results presented herein to investigate the cause of the $[N II]$ BPT diagram offset. Figure 13 shows the $[N II]$ and $[S II]$ BPT diagrams (Fig. 11) and the O_{32} vs. R_{23} , $O3N2$, and $N2$ diagrams (Fig. 12) with the $z \sim 2.3$ galaxies color-coded according to the magnitude of the offset in the $[N II]$ BPT diagram. We divided the $z \sim 2.3$ sample in the $[N II]$ BPT diagram at the running median $[O III]/H\beta$ in bins of $[N II]/H\alpha$, shown by the solid purple line in the top right panel. Galaxies above and to the right of this line in the $[N II]$ BPT diagram are shown in blue, while those galaxies that show a smaller offset and overlap the local sequence are shown in red. We have verified that our results do not change if other dividing lines in the $[N II]$ BPT diagram are used, including a linear fit and the best-fit line to the $z \sim 2.3$ star-forming sequence from Shapley et al. (2015) (red dashed line).

We find that the blue and red data points are well mixed and are not systematically offset from the local distribution in the O_{32} vs. R_{23} diagram. The running median of the three samples follow a very similar sequence where there is overlap at $\log(O_{32}) \sim -0.1$ to 0.4 . Similarly, the blue data points do not appear to follow a

different distribution from that of the red data points or the low-metallicity local sequence in the $[S II]$ BPT diagram. There is some separation in the two subsamples in the $[S II]$ BPT diagram because the blue data points have higher $[O III]/H\beta$ a priori due to the selection. In the $O3N2$ diagram, the red points fall close to the local distribution, while the blue points appear to be slightly more offset towards lower $O3N2$ at fixed O_{32} . The blue data points display less overlap with the red data points in the $N2$ diagram and a larger offset compared to local galaxies. We use the best-fit linear relations to the blue and red datapoints, respectively, to quantify the mean offsets and make the offsets clearer. The red line has a mean offset of -0.11 dex in $O3N2$ at fixed O_{32} compared to the local median, while the blue line is offset -0.30 dex on average. In the $N2$ diagram, the red and blue lines are offset 0.08 and 0.40 dex, respectively, towards higher $N2$ at fixed O_{32} .

To summarize, we find that, as a whole, the $z \sim 2.3$ sample shows no significant offset in line ratio diagrams that do not include nitrogen ($[S II]$ BPT and O_{32} vs. R_{23} diagrams). We find a slight offset in a diagram that utilizes a line ratio including nitrogen as well as oxygen (O_{32} vs. $O3N2$ diagram). This offset increases in the $N2$ diagram, in which nitrogen is the only metal species in the line ratio. Additionally, we find that galaxies showing the largest offset in the $[N II]$ BPT diagram do not distinguish themselves from galaxies showing a smaller offset when plotted in diagrams that do not include nitrogen. The most-offset galaxies in the $[N II]$ BPT diagram display systematically lower $O3N2$ values at fixed O_{32} than galaxies showing a small offset in the $[N II]$ BPT diagram. This effect increases in magnitude in the O_{32} vs. $N2$ diagram, in which those galaxies showing a large offset in the $[N II]$ BPT diagram display significantly larger $N2$ values at fixed O_{32} than the less-offset subsample of the $z \sim 2.3$ galaxies. A simple way to change the $[N II]/\lambda 6584$ flux without affecting the flux of the other strong optical emission lines is to change the nitrogen abundance. Our observations suggest that the N/O ratio at fixed O/H is higher on average in $z \sim 2.3$ star-forming galaxies compared to local star-forming galaxies. The high-redshift galaxies showing the largest offset in the $[N II]$ BPT di-

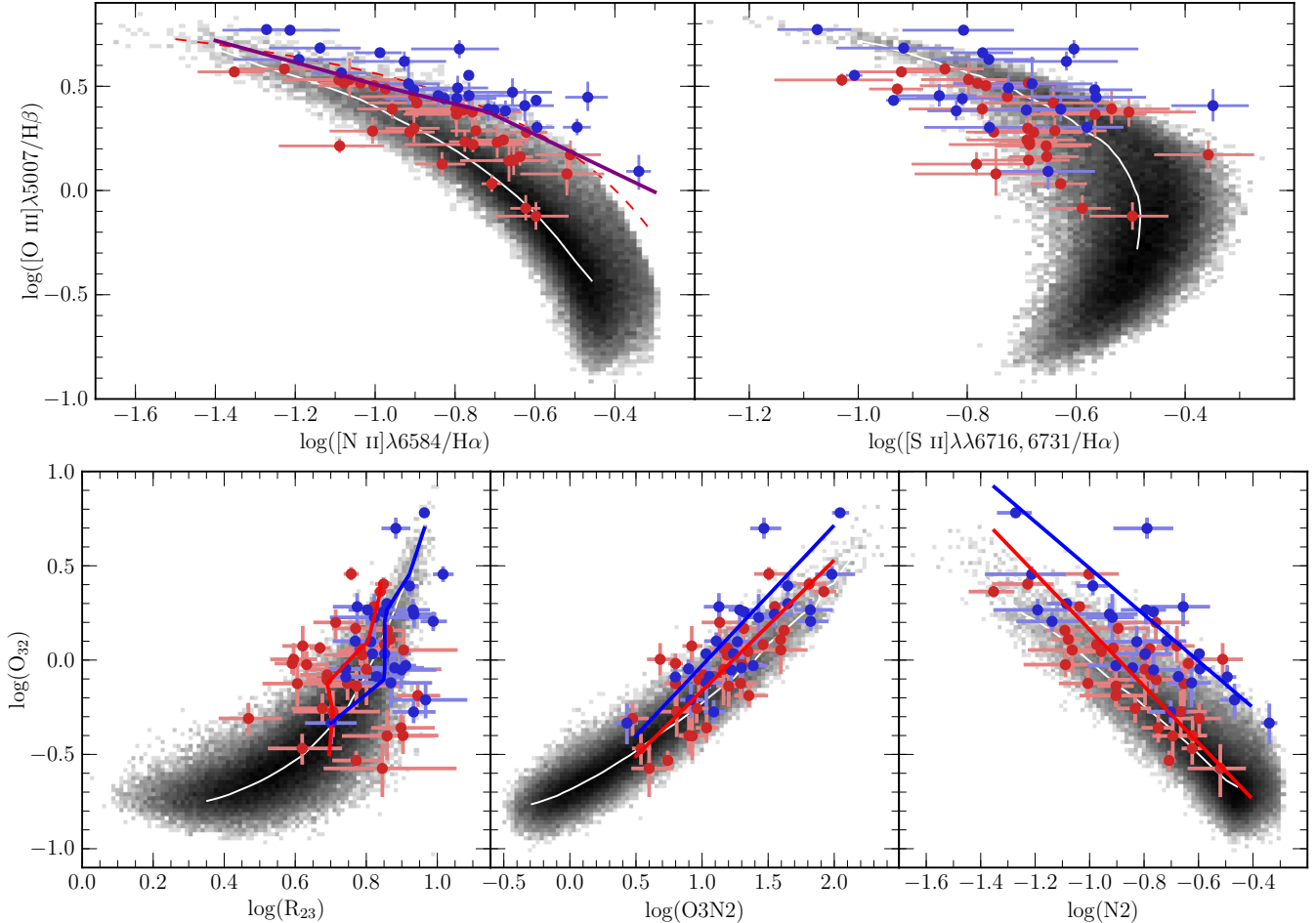


Figure 13. Emission line ratio diagrams with $z \sim 2.3$ galaxies color-coded by the offset in the [N II] BPT diagram. In each panel, the gray histogram shows the distribution of local star-forming galaxies from SDSS. The top row shows the [N II] (top left) and [S II] (top right) BPT diagrams. The O_{32} vs. R_{23} , O_{3N2} , and N_2 diagrams are shown in the left, middle, and right panels, respectively, of the bottom row. In each panel, the white line shows the running median of the $z \sim 0$ sample. In the top left panel, the solid purple line shows the running median of the $z \sim 2.3$ star-forming galaxies, while the dashed red line shows the fit to the MOSDEF $z \sim 2.3$ star-forming sequence from Shapley et al. (2015). In all panels, $z \sim 2.3$ galaxies falling above and to the right of the dashed red line are color-coded blue, while $z \sim 2.3$ galaxies falling below and to the left of this line are color-coded red. In the lower left panel, the red and blue curves show the median O_{32} in bins of O_{32} for the red and blue data points, respectively. The solid red and blue lines in the lower middle and right panels show the best linear fit to the red and blue data points, respectively. See Footnote 9 regarding the use of running medians and best-fit lines.

agram appear to have higher N/O ratios than less offset $z \sim 2.3$ galaxies of the same metallicity.

In Sections 5.1 and 5.2, we showed that our data are inconsistent with a systematically harder ionizing spectrum or higher ionization parameter in high-redshift galaxies at fixed metallicity. An increase in the gas density or ISM pressure can also move galaxies in the direction of the observed offset. We utilize Cloudy photoionization models to quantify the magnitude of this effect using the characteristic densities obtained in Section 3. Figure 14 shows the local star-forming sequence for reference, along with two photoionization model grids produced with the same ionizing spectrum (blackbody with $T_{\text{eff}} = 50,000$ K) while varying the electron density between 25 cm^{-3} and 250 cm^{-3} . The grids are shown over the metallicity range $0.2\text{--}0.6 Z_{\odot}$ in which the typical metallicity at $z \sim 2.3$ is expected to fall. The lowest metallicity grid points show negligible change in line ratios with density, while the dependence on density increases with metallicity. With an increase of a factor of 10 in density, $[O \text{ III}]/H\beta$ and $[N \text{ II}]/H\alpha$ are increased by

$\lesssim 0.1$ dex at fixed ionization parameter and metallicity. This is not a large enough shift to account for the observed offset in the [N II] BPT diagram. If our density estimate for local star-forming regions is underestimated, then the magnitude of the line ratio shift caused by density will be even smaller. Thus, the increase in density from $z \sim 0$ to $z \sim 2.3$ plays only a minor role in the [N II] BPT diagram offset.

We conclude that the observed offset of $z \sim 2.3$ galaxies from the local star-forming sequence in the [N II] BPT diagram is mostly caused by elevated N/O at fixed O/H compared to local galaxies, while an increase in density/pressure of the star-forming regions plays a minor role. We do not find evidence that a change in the ionizing spectrum or ionization parameter at fixed metallicity plays a part in the offset. This finding is consistent with earlier MOSDEF results from Shapley et al. (2015) attributing the offset in the BPT diagram to higher N/O in high-redshift galaxies with $M_{*} < 10^{10} M_{\odot}$. Our results are also in agreement with the interpretation of Masters et al. (2014), in which anomalous nitrogen abundance

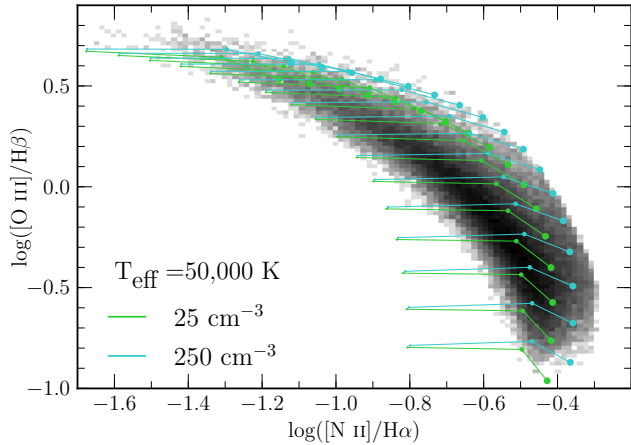


Figure 14. Model grids assuming a gas density of 25 cm^{-3} (light green) and 250 cm^{-3} (cyan) with gas-phase metallicity spanning $0.2\text{-}0.6 Z_{\odot}$ and an input ionizing spectrum of a $50,000 \text{ K}$ blackbody. Grid points are displayed as in Figure 11.

was first proposed as a cause of the offset. Steidel et al. (2014) also found an elevated N/O among their $z \sim 2.3$ sample, but argued that the primary cause of the offset lies in harder ionizing spectra and higher ionization parameters in comparison to what is observed locally.

The cause of the higher N/O ratios observed at high-redshift is not yet clear. Masters et al. (2014) speculated that a larger-than-normal population of Wolf-Rayet stars could produce a nitrogen enhancement, although a mechanism to produce such a population exclusively at high redshifts was not proposed. If the nitrogen enhancement is due to a significant difference in the stellar population at a given metallicity, there would likely be a difference in the overall ionizing spectrum that population produces, for which we do not see evidence. Another possibility is that gas flows lead to a larger nitrogen abundance at fixed O/H. If a large amount of unenriched gas is accreted and mixed into the star-forming regions before intermediate-mass stars enrich the ISM with nitrogen, O/H will decrease. The intermediate-mass stars will then release an amount of nitrogen that is larger than what is expected at that O/H because the gas is now less enriched than the stars. This scenario, or another mechanism involving gas inflows and outflows, is perhaps more likely in high-redshift galaxies which are known to have large gas fractions and concentrated star formation that could correspond to active accretion of metal-poor gas (Tacconi et al. 2013). We found evidence consistent with an accumulation of unenriched gas in $z \sim 2.3$ galaxies through the mass-metallicity relation in Sanders et al. (2015). Observations of the rest-frame UV could determine if exotic stellar populations are present, while more observations of the cold gas content of high-redshift galaxies with, e.g., ALMA could help uncover the role of gas flows.

The presence of AGN within the $z \sim 2.3$ sample could significantly bias conclusions drawn from excitation diagrams. We did not use a locally-determined demarcation to separate star-forming galaxies from AGN in the [N II] BPT diagram (e.g., Kewley et al. 2001; Kauffmann et al. 2003) because such a selection would introduce a bias against objects with high N/O at fixed [O III]/H β . While some of the galaxies in the $z \sim 2.3$ sample fall

in the local AGN region of the [N II] BPT diagram, we do not see any $z \sim 2.3$ galaxies present where the AGN sequence would fall in the other four panels of Figure 13. Therefore, we are confident that our $z \sim 2.3$ sample is free of AGN.

5.5. Diffuse ionized gas and the interpretation of global galaxy spectra

The observed positions of local and $z \sim 2.3$ galaxies in the [N II] and [S II] BPT diagrams are key pieces of evidence in our arguments regarding the hardness of the ionizing spectrum of local and high-redshift star-forming regions (see Section 5.1 and Figure 11). One source of uncertainty in the interpretation of these plots is the inclusion of light from the diffuse ionized component of the ISM in integrated-light galaxy spectra. Emission from diffuse ionized gas can be significant, with roughly half of the total H α emission of local spiral galaxies coming from a diffuse component (Zurita et al. 2000). If the diffuse ionized component has line ratios that are not equivalent to those of HII regions, which is probable because diffuse gas and HII regions are characterized by different ionizing sources and ionization states, then light from the diffuse component can act as a contaminant when investigating properties of star-forming regions. This issue is especially concerning for low ionization states such as [N II] and [S II] which are easily ionized and can have elevated flux compared to that of H α when shock-excited (Martin 1997; Hong et al. 2013). Characterizing the impact of diffuse emission requires knowledge of both the fraction of emission and the emission line ratios coming from the diffuse ionized component, at both low and high redshift.

In the local universe, comparison of integrated galaxy spectra with those of individual HII regions can give insight into the effect of emission from other components of the ISM. Local HII regions have been found to follow a similar sequence to that of local star-forming galaxies in the [N II] BPT diagram, but appear to have systematically lower [S II]/H α at fixed [O III]/H β in the [S II] BPT diagram (Veilleux & Osterbrock 1987; Pilyugin et al. 2012; Berg et al. 2015; Croxall et al. 2015). Every emission line in an integrated galaxy spectrum contains a luminosity-weighted contribution from each HII and diffuse emission region falling in the slit or fiber, complicating the comparison of HII region and integrated galaxy spectra. Ongoing spatially-resolved spectroscopic surveys, such as the SDSS-IV/MaNGA IFU (Law et al. 2015) and SAMI (Bryant et al. 2015) galaxy surveys, will provide a dataset capable of unraveling the relative contributions of HII regions and diffuse ionized gas to global galaxy spectra.

The situation is much more uncertain at high redshifts because the structure of the ISM in $z \sim 2$ galaxies is poorly constrained. The ISM is almost certainly different in $z \sim 2$ galaxies, considering the high gas fractions (Tacconi et al. 2013) and compact sizes (van der Wel et al. 2014), combined with high rates of star formation (Shivaei et al. 2015), significant feedback driving outflows (Shapley et al. 2003; Steidel et al. 2010), and high level of turbulence observed in $z \sim 2$ disk galaxies (Förster Schreiber et al. 2009). If high-redshift galaxies are dominated by giant kpc-scale HII regions ionized by super-star clusters that fill a large fraction of the galaxy volume,

the filling factor of the diffuse ionized component may be small along with the fraction of line emission originating there. In this case, it may be more appropriate to compare the integrated emission-line spectra of high-redshift galaxies to those of luminous local HII regions rather than global galaxy spectra. We are only starting to gain rudimentary knowledge of the spatially-resolved structure of the ionized ISM at $z \sim 2$ (Förster Schreiber et al. 2011; Genzel et al. 2011; Jones et al. 2013; Newman et al. 2014). Adaptive optics observations of increased sensitivity and spatial resolution will be required to map the spatially-resolved structure of the ionized component of the ISM at high redshift, including the strength of the [N II] and [S II] emission lines.

6. SUMMARY

We have investigated the physical conditions of star-forming regions at $z \sim 2.3$, specifically the electron density and ionization parameter, and made comparisons to local star-forming galaxies in order to understand how these properties evolve with redshift. We performed this investigation using rest-frame optical spectra of $z \sim 2.3$ galaxies from the ongoing MOSDEF survey. We summarize our main conclusions below and discuss future observations that could shed additional light on the ionization state of high-redshift galaxies.

1. We explored the evolution of the electron density in star-forming regions using the [O II] $\lambda\lambda 3726, 3729$ and [S II] $\lambda\lambda 6716, 6731$ doublets. We found that $z \sim 2.3$ galaxies have median [O II] $\lambda 3729/\lambda 3726 = 1.18$ and median [S II] $\lambda 6716/\lambda 6718 = 1.13$, corresponding to electron densities of 225 cm^{-3} and 290 cm^{-3} , respectively. Local star-forming galaxies from SDSS have median [S II] $\lambda 6716/\lambda 6718 = 1.41$ which yields a density of 26 cm^{-3} . We found an evolution in electron density of an order of magnitude between $z \sim 0$ and $z \sim 2.3$.
2. We investigated the ionization state of $z \sim 2.3$ and local star-forming galaxies, using O_{32} as a proxy for the ionization parameter. We found that O_{32} decreases with increasing stellar mass in both the local and $z \sim 2.3$ samples. The slope of the $O_{32}-M_*$ anti-correlation is very similar for both samples, but the $z \sim 2.3$ sample is offset ~ 0.6 dex higher in O_{32} relative to the local sample at fixed M_* . This offset can be explained by the evolution of the mass-metallicity relation with redshift, such that high-redshift galaxies have lower metallicities at fixed M_* , and the existence of an anti-correlation between ionization parameter and O/H.
3. We found that $z \sim 2.3$ galaxies show no systematic offset from local galaxies and follow the distribution of the low-metallicity tail of local galaxies in the O_{32} vs. R_{23} diagram. The high-redshift sample behaves similarly to the local sample in the O_{32} vs. $O3N2$ diagram, displaying a slight systematic offset from the local distribution. We propose that $z \sim 2.3$ galaxies follow the same anti-correlation between ionization parameter and O/H that is observed in the local universe.
4. Using simple photoionization models, we demonstrated that the translation between O_{32} and ionization parameter is only strongly dependent on the shape of the ionizing spectrum, and has little dependence on the assumed gas density and gas-phase metallicity. This translation will only evolve with redshift if the hardness of the ionizing spectrum at fixed metallicity evolves with redshift.
5. We utilized the position of $z \sim 2.3$ and local galaxies in the [N II] and [S II] BPT diagrams combined with simple photoionization models to show that the hardness of the ionizing spectrum does not significantly increase or decrease with redshift. Photoionization models predict that a hardening of the ionizing spectrum will increase [O III]/H β at fixed [N II]/H α and [S II]/H α . The $z \sim 2.3$ sample displays an offset from the local sequence in the [N II] BPT diagram but is not significantly offset in the [S II] BPT diagram. We conclude that there is not a significant increase in the hardness of the ionizing spectrum at fixed metallicity between $z \sim 0$ and $z \sim 2.3$.
6. Galaxies at $z \sim 2.3$ show no significant systematic offset from local galaxies in line ratio diagrams involving only lines of oxygen, sulfur, and hydrogen, while they show a systematic offset in line ratio diagrams involving nitrogen. These results suggest that metallicity indicators using line ratios excluding nitrogen (e.g. the combination of O_{32} and R_{23}) do not evolve up to $z \sim 2.3$, while indicators using nitrogen are biased due to an evolution in N/O at fixed O/H.
7. A consequence of conclusions 6 and 7 is that $z \sim 2.3$ have similar ionization parameters to $z \sim 0$ galaxies at fixed metallicity. Higher typical ionization parameters are inferred for $z \sim 2.3$ galaxies compared to those of local galaxies because $z \sim 2.3$ galaxies have lower typical metallicities. The ionization state appears to be set by the metallicity both locally and at $z \sim 2.3$.
8. We investigated the offset between $z \sim 2.3$ and local galaxies in the [N II] BPT diagram. We found that the $z \sim 2.3$ galaxies that display the largest offsets in the [N II] BPT diagram are not significantly offset from the local distribution or the remainder of the $z \sim 2.3$ sample in the O_{32} vs. R_{23} and [S II] BPT diagrams, but are systematically offset in the O_{32} vs. $O3N2$ and $N2$ diagrams. We conclude that higher N/O at fixed O/H drives the $z \sim 2.3$ offset in the [N II] BPT diagram. We previously provided evidence against significant evolution of the hardness of the ionizing spectrum or ionization parameter at fixed O/H. We used simple photoionization models to show that an evolution of a factor of 10 in the gas density cannot account for the full offset in the [N II] BPT diagram. We further conclude that an increase in the gas density plays a minor secondary role in driving the $z \sim 2.3$ offset in the [N II] BPT diagram.

There still remain many questions to be answered regarding the ionization state of local and $z \sim 2.3$ galax-

ies. Emission line contribution from the diffuse ionized component of the ISM is uncertain both locally and at high redshifts. Variety in photoionization modeling leads to variation in estimated ionization parameters. There are some observations that would allow us to test our proposed scenario that $z \sim 2.3$ galaxies have the same ionization parameter as $z \sim 0$ galaxies with the same metallicity. The most obvious of these is direct-method oxygen abundance measurements from auroral lines at $z \sim 2$. Direct-method abundances are insensitive to changes in the electron density, showing variations of $\lesssim 0.01$ dex from 25 cm^{-3} to 250 cm^{-3} (i.e., the observed evolution in density from $z \sim 0$ to $z \sim 2.3$), an advantage over some strong-line methods (see Jones et al. 2015). Currently, only a handful of direct-method abundance measurements have been attained at $z \gtrsim 1$, often utilizing gravitational lensing (Villar-Martín et al. 2004; Yuan & Kewley 2009; Erb et al. 2010; Rigby et al. 2011; Brammer et al. 2012b; Christensen et al. 2012; Maseda et al. 2014). Current sensitive near-infrared spectrographs on 10 m class telescopes and upcoming instruments on the Thirty Meter Telescope will allow for observations of auroral lines for more typical galaxies at $z > 1$. Additionally, observations of other ionization-parameter-sensitive emission line ratios could provide a test of this scenario, including $[\text{Ne III}]\lambda 3869/[\text{O II}]\lambda\lambda 3726, 3729$ (Levesque & Richardson 2014) and $[\text{S III}]\lambda\lambda 9069, 9532/[\text{S II}]\lambda\lambda 6716, 6731$ (Kewley & Dopita 2002). Finally, improved stellar and photoionization models that can make self-consistent predictions of the physical properties of star-forming galaxies across the entire local star-forming sequence are needed to create more reliable ionization parameter calibrations. Such models would provide a local foundation for reliable photoionization models of the full suite of strong rest-frame optical emission lines out to $z \sim 2$.

We thank Tucker Jones for enlightening conversations, and acknowledge the First Carnegie Symposium in Honor of Leonard Searle for useful information and discussions that benefited this work. We acknowledge support from NSF AAG grants AST-1312780, 1312547, 1312764, and 1313171, and archival grant AR-13907, provided by NASA through the Space Telescope Science Institute. We are also grateful to Marc Kassis at the Keck Observatory for his many valuable contributions to the execution of the MOSDEF survey. We also acknowledge the 3D-HST collaboration, who provided us with spectroscopic and photometric catalogs used to select MOSDEF targets and derive stellar population parameters. We also thank I. McLean, K. Kulas, and G. Mace for taking observations for the MOSDEF survey in May and June 2013. MK acknowledges support from the Hellmann Fellows fund. ALC acknowledges funding from NSF CAREER grant AST-1055081. NAR is supported by an Alfred P. Sloan Research Fellowship. We wish to extend special thanks to those of Hawaiian ancestry on whose sacred mountain we are privileged to be guests. Without their generous hospitality, most of the observations presented herein would not have been possible. This work is also based on observations made with the NASA/ESA Hubble Space Telescope, which is operated by the Association of Universities for Research in Astronomy, Inc.,

under NASA contract NAS 5-26555. Observations associated with the following GO and GTO programs were used: 12063, 12440, 12442, 12443, 12444, 12445, 12060, 12061, 12062, 12064 (PI: Faber); 12177 and 12328 (PI: van Dokkum); 12461 and 12099 (PI: Riess); 11600 (PI: Weiner); 9425 and 9583 (PI: Giavalisco); 12190 (PI: Koekemoer); 11359 and 11360 (PI: OConnell); 11563 (PI: Illingworth).

REFERENCES

- Abazajian, K. N., Adelman-McCarthy, J. K., Agüeros, M. A., et al. 2009, *ApJS*, 182, 543
- Andrews, B. H., & Martini, P. 2013, *ApJ*, 765, 140
- Asplund, M., Grevesse, N., Sauval, A. J., & Scott, P. 2009, *ARA&A*, 47, 481
- Belli, S., Jones, T., Ellis, R. S., & Richard, J. 2013, *ApJ*, 772, 141
- Berg, D. A., Skillman, E. D., Croxall, K. V., et al. 2015, *ApJ*, 806, 16
- Bian, F., Fan, X., Bechtold, J., et al. 2010, *ApJ*, 725, 1877
- Brammer, G. B., van Dokkum, P. G., Franx, M., et al. 2012a, *ApJS*, 200, 13
- Brammer, G. B., Sánchez-Janssen, R., Labbé, I., et al. 2012b, *ApJ*, 758, L17
- Bresolin, F., Kennicutt, R. C., & Ryan-Weber, E. 2012, *ApJ*, 750, 122
- Brinchmann, J., Pettini, M., & Charlot, S. 2008, *MNRAS*, 385, 769
- Bryant, J. J., Owers, M. S., Robotham, A. S. G., et al. 2015, *MNRAS*, 447, 2857
- Calzetti, D., Armus, L., Bohlin, R. C., et al. 2000, *ApJ*, 533, 682
- Cardelli, J. A., Clayton, G. C., & Mathis, J. S. 1989, *ApJ*, 345, 245
- Chabrier, G. 2003, *PASP*, 115, 763
- Christensen, L., Laursen, P., Richard, J., et al. 2012, *MNRAS*, 427, 1973
- Coil, A. L., Aird, J., Reddy, N., et al. 2015, *ApJ*, 801, 35
- Conroy, C., Gunn, J. E., & White, M. 2009, *ApJ*, 699, 486
- Croxall, K. V., Pogge, R. W., Berg, D. A., Skillman, E. D., & Moustakas, J. 2015, *ApJ*, 808, 42
- Cullen, F., Cirasuolo, M., McLure, R. J., Dunlop, J. S., & Bowler, R. A. A. 2014, *MNRAS*, 440, 2300
- Díaz, A. I., Castellanos, M., Terlevich, E., & Luisa García-Vargas, M. 2000, *MNRAS*, 318, 462
- Dopita, M. A., & Evans, I. N. 1986, *ApJ*, 307, 431
- Dopita, M. A., Sutherland, R. S., Nicholls, D. C., Kewley, L. J., & Vogt, F. P. A. 2013, *ApJS*, 208, 10
- Dopita, M. A., Fischera, J., Sutherland, R. S., et al. 2006a, *ApJ*, 647, 244
- , 2006b, *ApJS*, 167, 177
- Dors, Jr., O. L., Krabbe, A., Hägele, G. F., & Pérez-Montero, E. 2011, *MNRAS*, 415, 3616
- Ekström, S., Georgy, C., Eggenberger, P., et al. 2012, *A&A*, 537, A146
- Eldridge, J. J., Langer, N., & Tout, C. A. 2011, *MNRAS*, 414, 3501
- Eldridge, J. J., & Stanway, E. R. 2012, *MNRAS*, 419, 479
- Erb, D. K., Pettini, M., Shapley, A. E., et al. 2010, *ApJ*, 719, 1168
- Erb, D. K., Shapley, A. E., Pettini, M., et al. 2006, *ApJ*, 644, 813
- Esteban, C., Bresolin, F., Peimbert, M., et al. 2009, *ApJ*, 700, 654
- Esteban, C., Carigi, L., Copetti, M. V. F., et al. 2013, *MNRAS*, 433, 382
- Esteban, C., García-Rojas, J., Carigi, L., et al. 2014, *MNRAS*, 443, 624
- Ferland, G. J., Porter, R. L., van Hoof, P. A. M., et al. 2013, *RMxAA*, 49, 137
- Fischer, C. F., & Tachiev, G. 2014, MCHF/MCDHF Collection, Version 2, Ref No. 10 & 20, Available online at <http://physics.nist.gov/mchf>, National Institute of Standards and Technology
- Förster Schreiber, N. M., Genzel, R., Bouché, N., et al. 2009, *ApJ*, 706, 1364
- Förster Schreiber, N. M., Shapley, A. E., Genzel, R., et al. 2011, *ApJ*, 739, 45

- García-Rojas, J., Esteban, C., Peimbert, A., et al. 2005, *MNRAS*, 362, 301
— 2007, *RMxAA*, 43, 3
García-Rojas, J., Esteban, C., Peimbert, M., et al. 2006, *MNRAS*, 368, 253
García-Rojas, J., Simón-Díaz, S., & Esteban, C. 2014, *A&A*, 571, A93
Genzel, R., Newman, S., Jones, T., et al. 2011, *ApJ*, 733, 101
Georgy, C., Ekström, S., Eggenberger, P., et al. 2013, *A&A*, 558, A103
Grogin, N. A., Kocevski, D. D., Faber, S. M., et al. 2011, *ApJS*, 197, 35
Hainline, K. N., Shapley, A. E., Kornei, K. A., et al. 2009, *ApJ*, 701, 52
Henry, A., Scarlata, C., Domínguez, A., et al. 2013, *ApJ*, 776, L27
Holden, B. P., Oesch, P. A., Gonzalez, V. G., et al. 2014, *ArXiv e-prints*, arXiv:1401.5490
Hong, S., Calzetti, D., Gallagher, III, J. S., et al. 2013, *ApJ*, 777, 63
Hopkins, A. M., & Beacom, J. F. 2006, *ApJ*, 651, 142
Jones, T., Ellis, R. S., Richard, J., & Jullo, E. 2013, *ApJ*, 765, 48
Jones, T., Martin, C., & Cooper, M. C. 2015, *ArXiv e-prints*, arXiv:1504.02417
Kauffmann, G., Heckman, T. M., Tremonti, C., et al. 2003, *MNRAS*, 346, 1055
Kennicutt, Jr., R. C. 1984, *ApJ*, 287, 116
— 1998, *ARA&A*, 36, 189
Kewley, L. J., & Dopita, M. A. 2002, *ApJS*, 142, 35
Kewley, L. J., Dopita, M. A., Leitherer, C., et al. 2013a, *ApJ*, 774, 100
Kewley, L. J., Dopita, M. A., Sutherland, R. S., Heisler, C. A., & Trevena, J. 2001, *ApJ*, 556, 121
Kewley, L. J., & Ellison, S. L. 2008, *ApJ*, 681, 1183
Kewley, L. J., Maier, C., Yabe, K., et al. 2013b, *ApJ*, 774, L10
Koekemoer, A. M., Faber, S. M., Ferguson, H. C., et al. 2011, *ApJS*, 197, 36
Kriek, M., van Dokkum, P. G., Labbé, I., et al. 2009, *ApJ*, 700, 221
Kriek, M., Shapley, A. E., Reddy, N. A., et al. 2015, *ApJS*, 218, 15
Lara-López, M. A., Hopkins, A. M., López-Sánchez, A. R., et al. 2013, *MNRAS*, 434, 451
Law, D. R., Yan, R., Bershad, M. A., et al. 2015, *AJ*, 150, 19
Lehnert, M. D., Nesvadba, N. P. H., Le Tiran, L., et al. 2009, *ApJ*, 699, 1660
Leitherer, C., Ekström, S., Meynet, G., et al. 2014, *ApJS*, 212, 14
Lequeux, J., Peimbert, M., Rayo, J. F., Serrano, A., & Torres-Peimbert, S. 1979, *A&A*, 80, 155
Levesque, E. M., & Richardson, M. L. A. 2014, *ApJ*, 780, 100
Liu, X., Shapley, A. E., Coil, A. L., Brinchmann, J., & Ma, C.-P. 2008, *ApJ*, 678, 758
López-Sánchez, Á. R., Esteban, C., García-Rojas, J., Peimbert, M., & Rodríguez, M. 2007, *ApJ*, 656, 168
Madau, P., & Dickinson, M. 2014, *ARA&A*, 52, 415
Maiolino, R., Nagao, T., Grazian, A., et al. 2008, *A&A*, 488, 463
Mannucci, F., Cresci, G., Maiolino, R., Marconi, A., & Gnerucci, A. 2010, *MNRAS*, 408, 2115
Martin, C. L. 1997, *ApJ*, 491, 561
Maseda, M. V., van der Wel, A., Rix, H.-W., et al. 2014, *ArXiv e-prints*, arXiv:1406.3351
Masters, D., McCarthy, P., Siana, B., et al. 2014, *ApJ*, 785, 153
McLean, I. S., Steidel, C. C., Epps, H. W., et al. 2012, in *Society of Photo-Optical Instrumentation Engineers (SPIE) Conference Series*, Vol. 8446, *Society of Photo-Optical Instrumentation Engineers (SPIE) Conference Series*
Nakajima, K., & Ouchi, M. 2014, *MNRAS*, 442, 900
Nakajima, K., Ouchi, M., Shimasaku, K., et al. 2013, *ApJ*, 769, 3
Newman, S. F., Buschkamp, P., Genzel, R., et al. 2014, *ApJ*, 781, 21
Nicholls, D. C., Dopita, M. A., Sutherland, R. S., Kewley, L. J., & Palay, E. 2013, *ApJS*, 207, 21
Osterbrock, D. E., & Ferland, G. J. 2006, *Astrophysics of gaseous nebulae and active galactic nuclei*
Peimbert, A., Peña-Guerrero, M. A., & Peimbert, M. 2012, *ApJ*, 753, 39
Pellegrini, E. W., Baldwin, J. A., & Ferland, G. J. 2011, *ApJ*, 738, 34
Pérez-Montero, E. 2014, *MNRAS*, 441, 2663
Pérez-Montero, E., & Contini, T. 2009, *MNRAS*, 398, 949
Pettini, M., & Pagel, B. E. J. 2004, *MNRAS*, 348, L59
Pilyugin, L. S., Vílchez, J. M., Mattsson, L., & Thuan, T. X. 2012, *MNRAS*, 421, 1624
Reddy, N. A., Pettini, M., Steidel, C. C., et al. 2012, *ApJ*, 754, 25
Reddy, N. A., Kriek, M., Shapley, A. E., et al. 2015, *ApJ*, 806, 259
Reynolds, R. J. 1985, *ApJ*, 294, 256
Rigby, J. R., Wuyts, E., Gladders, M. D., Sharon, K., & Becker, G. D. 2011, *ApJ*, 732, 59
Salpeter, E. E. 1955, *ApJ*, 121, 161
Sánchez, S. F., Pérez, E., Rosales-Ortega, F. F., et al. 2015, *A&A*, 574, A47
Sanders, R. L., Shapley, A. E., Kriek, M., et al. 2015, *ApJ*, 799, 138
Shapley, A. E., Coil, A. L., Ma, C.-P., & Bundy, K. 2005, *ApJ*, 635, 1006
Shapley, A. E., Steidel, C. C., Pettini, M., & Adelberger, K. L. 2003, *ApJ*, 588, 65
Shapley, A. E., Reddy, N. A., Kriek, M., et al. 2015, *ApJ*, 801, 88
Shaw, R. A., & Dufour, R. J. 1994, in *Astronomical Society of the Pacific Conference Series*, Vol. 61, *Astronomical Data Analysis Software and Systems III*, ed. D. R. Crabtree, R. J. Hanisch, & J. Barnes, 327
Shimakawa, R., Kodama, T., Steidel, C. C., et al. 2015, *MNRAS*, 451, 1284
Shirazi, M., Brinchmann, J., & Rahmati, A. 2014, *ApJ*, 787, 120
Shivaei, I., Reddy, N. A., Shapley, A. E., et al. 2015, *ArXiv e-prints*, arXiv:1507.03017
Skelton, R. E., Whitaker, K. E., Momcheva, I. G., et al. 2014, *ArXiv e-prints*, arXiv:1403.3689
Steidel, C. C., Erb, D. K., Shapley, A. E., et al. 2010, *ApJ*, 717, 289
Steidel, C. C., Rudie, G. C., Strom, A. L., et al. 2014, *ApJ*, 795, 165
Storey, P. J., & Zeppen, C. J. 2000, *MNRAS*, 312, 813
Stott, J. P., Sobral, D., Bower, R., et al. 2013, *MNRAS*, 436, 1130
Tacconi, L. J., Neri, R., Genzel, R., et al. 2013, *ApJ*, 768, 74
Tayal, S. S. 2007, *ApJS*, 171, 331
Tayal, S. S., & Zatsarinny, O. 2010, *ApJS*, 188, 32
Tremonti, C. A., Heckman, T. M., Kauffmann, G., et al. 2004, *ApJ*, 613, 898
Troncoso, P., Maiolino, R., Sommariva, V., et al. 2014, *A&A*, 563, A58
van der Wel, A., Franx, M., van Dokkum, P. G., et al. 2014, *ApJ*, 788, 28
van Zee, L., & Haynes, M. P. 2006, *ApJ*, 636, 214
Veilleux, S., & Osterbrock, D. E. 1987, *ApJS*, 63, 295
Villar-Martín, M., Cerviño, M., & González Delgado, R. M. 2004, *MNRAS*, 355, 1132
Watson, C., Povich, M. S., Churchwell, E. B., et al. 2008, *ApJ*, 681, 1341
Whitaker, K. E., Franx, M., Leja, J., et al. 2014, *ApJ*, 795, 104
Wright, S. A., Larkin, J. E., Graham, J. R., & Ma, C.-P. 2010, *ApJ*, 711, 1291
York, D. G., Adelman, J., Anderson, Jr., J. E., et al. 2000, *AJ*, 120, 1579
Yuan, T.-T., & Kewley, L. J. 2009, *ApJ*, 699, L161
Zurita, A., Rozas, M., & Beckman, J. E. 2000, *A&A*, 363, 9